UNIVERSITY OF CALIFORNIA

SANTA CRUZ

NANOSCALE REACTIVE ION ETCHING OF SILICON NITRIDE THIN FILMS FOR EMBEDDED NANOMAGNETIC DEVICE FABRICATION

A thesis submitted in partial satisfaction
of the requirements for the degree of

MASTER OF SCIENCE

in

ELECTRICAL ENGINEERING

by

David Luke Hibbard-Lubow

December 2017

The Thesis of David Luke Hibbard-Lubow
is approved:

_____
Professor Holger Schmidt, Chair

_____
Professor Nobuhiko P. Kobayashi

_____
Professor Ahmet Ali Yanik

_____
Tyrus Miller
Vice Provost and Dean of Graduate Studies

Contents

List of Figures

1 Abstract

Nanoscale Reactive Ion Etching of Silicon Nitride Thin Films for Embedded Nanomagnetic Device Fabrication

David Luke Hibbard-Lubow

The demands of digital memory have increased exponentially in recent history, requiring faster, smaller and more accurate storage methods. Two promising solutions to this ever-present problem are Bit Patterned Media (BPM) and Spin-Transfer Torque Magnetic Random Access Memory (STT-MRAM). Producing these technologies requires difficult and expensive fabrication techniques. Thus, the production processes must be optimized to allow these storage methods to compete commercially while continuing to increase their information storage density and reliability. I developed a process for the production of nanomagnetic devices (which can take the form of several types of digital memory) embedded in thin silicon nitride films. My focus was on optimizing the reactive ion etching recipe required to embed the device in the film. Ultimately, I found that recipe 37 (Power: 250W, CF_4 nominal/actual flow rate: 25/25.4 sccm, O_2 nominal/actual flow rate: 3.1/5.2 sccm, which gave a maximum pressure around 400 mTorr) gave the most repeatable and anisotropic results. I successfully used processes described in this thesis to make embedded nanomagnets, which could be used as bit patterned media. Another promising application of this work is to make embedded magnetic tunneling junctions, which are the storage medium used in MRAM. Doing so will require still some tweaks to the fabrication methods. Techniques for making these changes and their potential effects are discussed.

2 Acknowledgments

I would like to thank Professor Holger Schmidt for recognizing my potential and encouraging me to pursue a graduate degree. Without the opportunities he provided me and his willingness to help me find a way to work toward my degree without compromising my professional goals, I never would have continued my education. My work, and ultimately my thesis, would not have been possible without the efforts of our Lab Manager and Project Scientist, Dr. Thomas Yuzvinsky. His suggestions and brilliant problem solving abilities proved invaluable to my work in the Applied Optics Group. I would like to thank Dr. Weigang Yang and Mike Jaris. They both took time away from their work to teach me the intricacies of the theory behind my work and explain the operating procedures for the machines I needed to us to make my samples. Lastly, I would like to thank Cassidy Berk for providing vital discussion and interpretations of my results.

3 Introduction

3.1 Novel Storage Technologies

BPM stores bits of information on isolated nanomagnetic dots rather than the arbitrarily arranged magnetic grains of current hard disc drives. This could allow BPM to solve many of the problems faced by conventional magnetic grain-based storage. However, the large-scale fabrication of BPM requires several novel and difficult processes, hindering commercialization [1]. The research presented in this thesis focuses in part on optimizing the processes involved in the production of nanomagnetic arrays that are candidates for commercial BPM.

Bit patterned media consists of arrays of nanomagnetic dots, each storing a digital bit of information, with the value determined by the direction of its magnetization. This differs from a magnetic grain-based method, where multiple adjacent grains are magnetized in the same direction to form one bit, which leads to somewhat random variation in the size, shape and number of grains representing one bit. This limits the minimum size of bits, determined by their potential for increasing the error rate and thermal instability [1].

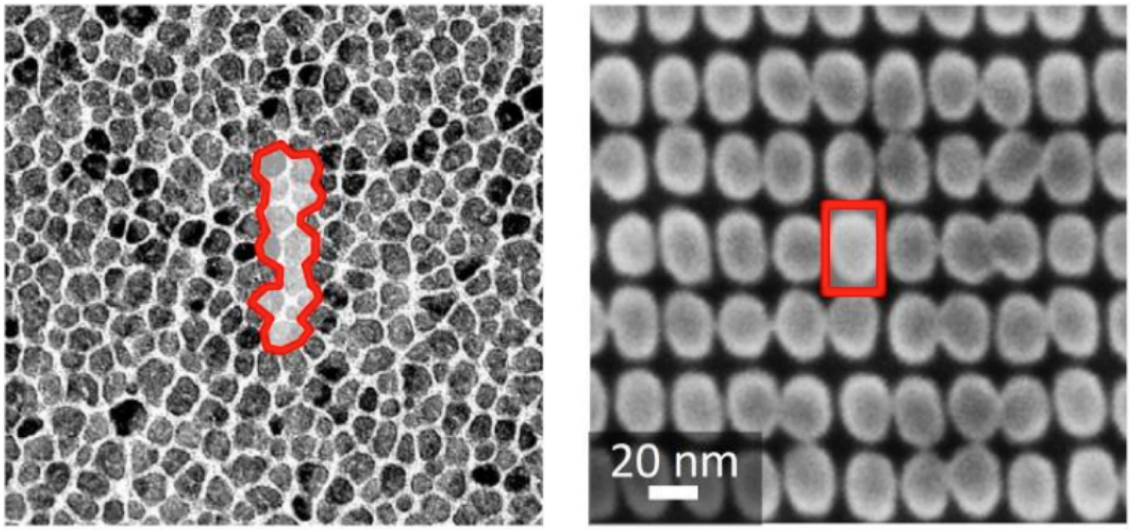

Figure 1: A comparison of traditional magnetic grain-based storage (left) to BPM (right) [1]. The red outline represents one bit and the scale bar is the same for both images.

As can be seen in figure 1, a BPM bit is significantly smaller in at least one direction than the multi-grain bit, allowing more information to be stored in a smaller space. However, BPM could only ever replace hard disk drives (HDDs), because BPM is simply too slow to function as the other types of memory used by computers.

STT-MRAM, on the other hand, has the potential to replace the four standard types of memory currently used by computers (DRAM, SRAM, flash, and HDD) [2]. This could reduce the communication needed between different types of memory, potentially improving speed and reducing power consumption. Thus, STT-MRAM is a much more widely applicable and promising technology and its production (in an information dense and low cost manner) is the long-term goal of the research

discussed in this thesis.

The principle behind STT-MRAM revolves around magnetic tunneling junctions (MTJs), which are used to store the digital information. Thus, a comprehension of MTJs is necessary before STT-MRAM can be understood. In addition, MTJs are the focus of much of the research discussed in this thesis. Thus, an explanation of the physics behind MTJs is presented here, followed by a discussion of their potential applications (including STT-MRAM).

Magnetic Tunneling Junctions (MTJs), in their simplest form, are made of two magnetic layers separated by a thin insulating layer. Typically, the top film is referred to as the free layer. As the name implies, its magnetic orientation is free to change, relative to that of the bottom layer. The magnetization of the bottom layer is fixed, so it is appropriately called the fixed or reference layer.

When an MTJ is used as part of a storage technology, a bit of digital information (a 1 or a 0) is stored as the orientation of the free layer's magnetization, relative to that of the fixed layer. Such a device has two basic magnetic states: parallel and antiparallel, which refers to the relative alignment of the magnetizations of the free and reference layers and corresponds to a 1 or 0, in terms of digital information. A depiction of these states and their effects on the energy bands can be seen in figure 2.

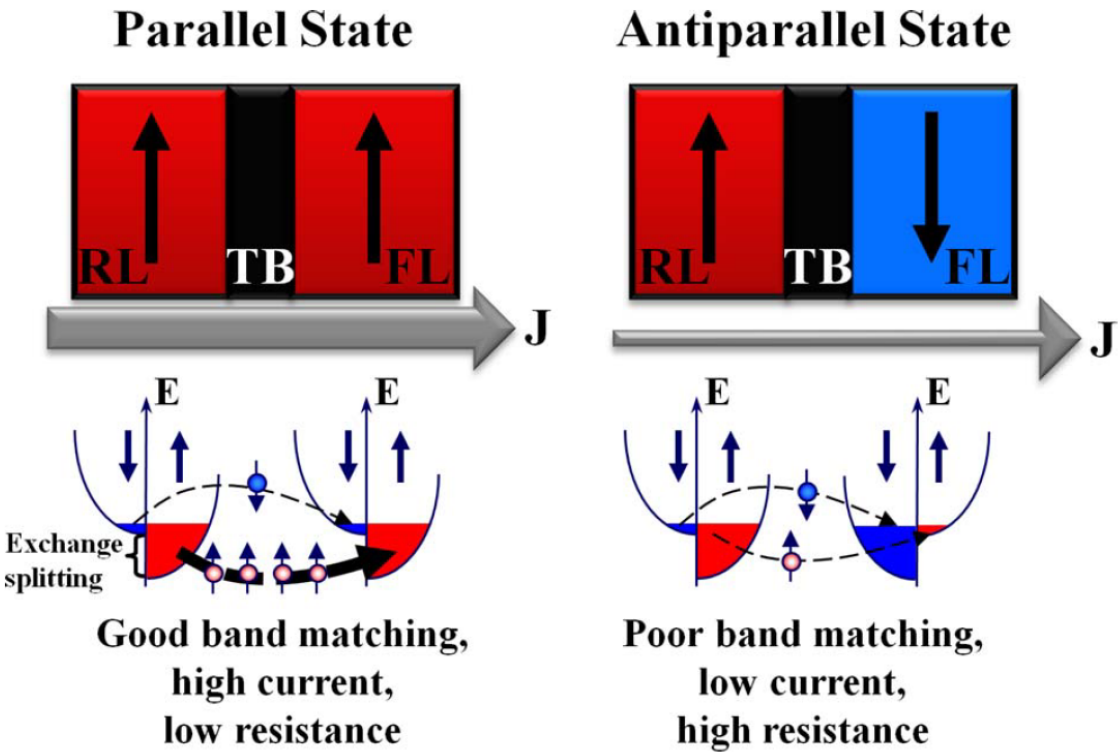

Figure 2: The basic structure of an MTJ in its parallel and antiparallel states, along with the resulting bands [3]. RL: reference layer; TB: tunnel barrier; FL: free layer.

In a well designed MTJ, the insulating barrier is thin enough that electrons can tunnel from one side to the other. However, the ease with which they can do so is greatly influenced by the relative orientation of the magnetizations of the free and reference layers. As one might expect, if the magnetizations are antiparallel, it is several times more difficult for electrons to tunnel from one layer to another compared to the parallel state. This difficulty is manifested as tunnelling magnetoresistance (TMR), and can be measured, allowing the bit to be read.

Conventionally, the value of the bit was changed by applying a current-generated magnetic field to the free layer, thus changing it from a parallel to an antiparallel state, or vice versa. This method was adapted from traditional hard disk drive (HDD) writing techniques and was not as effective as the spin transfer torque (STT) writing method, which has since become the norm.

STT works by creating a current of electrons whose spins are all aligned in a specific direction. This current then flows through the MTJ and the electrons transfer their spin angular momentum to the free layer, providing it with the angular momentum necessary to flip its magnetic orientation and thus changing the value of the bit of information it stores [4]. The position of an MTJ within the basic structure of STT-MRAM can be seen in figure 3.

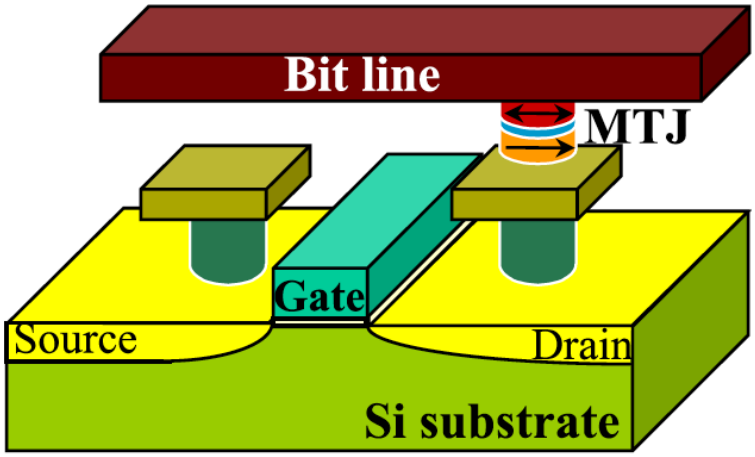

Figure 3: A schematic of an MTJ used in STT-MRAM [3].

Thus, MTJs are an integral part of MRAM, but they have a myriad of potential other applications, including acting as nanoscale spintronic oscillators, potentially

as a substitute for neural networks in emerging computational fields like speech recognition [5].

3.2 Embedded vs. On-Surface Devices

Embedded memory technologies are a novel solution to the many problems that arise from the fabrication of traditional types of on-surface memory. Specifically, on-surface STT-MRAM is expensive to fabricate, and the current methods used to do so can often lead to a relatively high MTJ failure rate [6]. Embedding the MTJ in the substrate via etching offers a potential solution to these problems [7] and provides increased scalability and versatility [8]. In addition, embedding MTJs in the substrate could allow for easier integration of STT-MRAM with other elements of a standard computer [9], allowing for increased performance.

Thus, much of the work presented in this thesis involves embedding MTJs and other nanomagnetic devices in substrates.

3.3 Reactive Ion Etching

Reactive ion etchers (RIE) are commonly used for etching silicon or silicon-based compounds, such as silicon nitride (Si_3N_4). Typically, these etches are done to depths of microns. On such a scale, RIEs provide predictable depths and highly anisotropic (vertical) etches.

A diagram of the basic components of an RIE can be seen in figure 4.

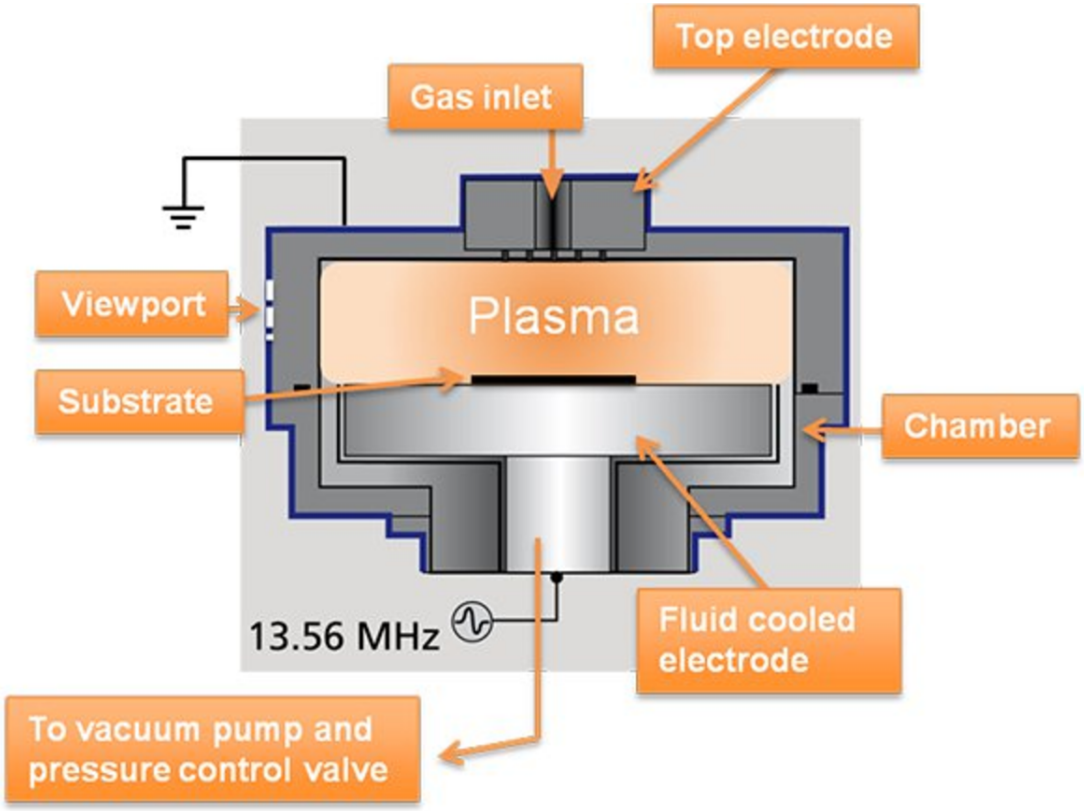

Figure 4: A schematic of the essential parts of a reactive ion etcher [10].

To etch a sample, it is loaded into the chamber, which is then pumped down to a few hundred mTorr. The etchant gas(es) then flow in through the gas inlet until the pressure stabilizes. An AC field with a frequency of 13.56 MHz is applied to the bottom electrode, typically with a few hundred watts of power.

This AC field causes the gas molecules to oscillate. Since the nuclei of the atoms are positively charged and the electrons are negatively charged, they are pulled in opposite directions. Additionally, their differences in mass cause them to oscillate

with different amplitudes. The net result is that the molecules are stripped of their electrons, creating a plasma of positive ions and free electrons.

As the free electrons are oscillate, some stick to the bottom electrode, and some to the top electrode. Since the top electrode is grounded, the electrons that hit it are quickly removed. However, the bottom electrode is electrically isolated, so the electrons that come in contact with it deposit a net negative charge, creating a potential difference between the top and bottom electrodes.

This voltage causes the positive ions to accelerate toward the bottom electrode. Some of them hit the sample (which is resting on the bottom electrode). The ions form bonds with the sample's molecules, causing them to separate from the sample. They are then removed by the vacuum pump. Ions can also remove parts of the sample via physical sputtering, using purely kinetic energy to break some of the bonds holding the sample's atoms in place. [11] [12].

In order to control the type and rate of the etch, the user can vary the gas content, pressure and power, though changing one of these often changes the others.

3.4 Scanning Electron Microscopy

Electronic and computational technologies are getting smaller at an exponential rate. To produce and examine these devices, we must go beyond the physical size limits of traditional confocal microscopy. A key tool in this push for miniaturization is the scanning electron microscope (SEM). As the name implies, SEMs use electrons, rather than photons, to examine samples.

The decision to use electrons comes from the fundamental resolution limit set

forward by the Rayleigh criteria, which ultimately gives the lateral resolution as proportional to the wavelength. Due to their mass, electrons can have lower wavelengths than photons. Thus, they allow the SEM user to resolve smaller features than would photons [13].

In addition, SEMs can be used to do lithography on a nanometer scale, called electron beam lithography (EBL). This process is detailed later in the Targeted Etching via Electron Beam Lithography section, but it replaces the light used for traditional lithography with a highly focused electron beam. This beam exposes the photoresist in the desired pattern, so that material can be adhered to the substrate only in the requisite locations. This process is essential to the method of embedded nanomagnet fabrication used to make the devices examined in this thesis.

4 Experimental Methods

4.1 Targeted Etching via Electron Beam Lithography

As mentioned in the previous section, electron beam lithography is essential to the fabrication of nanodevices. However, to embed them in the substrate, an etch is also needed. A depiction of this process can be seen in the figure 5. I start with a bare silicon substrate (which is doped when I am attempting to make a real MTJ). Through a collaboration with Brigham Young University, these substrates are then coated with a $\sim$50nm Si_3N_4 film using chemical vapor deposition (CVD). I then spin coat the sample with a $\sim$200nm thick layer of PMMA 950, which is a photoresist that responds to electrons. Next, I selectively expose the PMMA, using an electron

beam. I remove the exposed PMMA with a development step and etch into the Si_3N_4 film (and a bit into the doped Si to ensure electrical contact) using an RIE. Note that the etching process does not significantly affect the remaining PMMA or etch the material below it, by design. I deposit metal with an electron beam evaporator, or send the sample off to have an MTJ stack deposited on it via sputtering. Lastly, I use a liftoff step to remove any metal that is on top of the PMMA (not in the area exposed by the electron beam), leaving only the embedded devices. To evaluate the results, I take images of the sample with the SEM and/or an atomic force microscope (AFM), which precisely measures the topology.

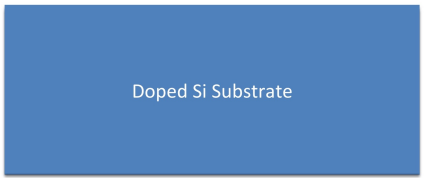

(a) Bare doped silicon substrate.

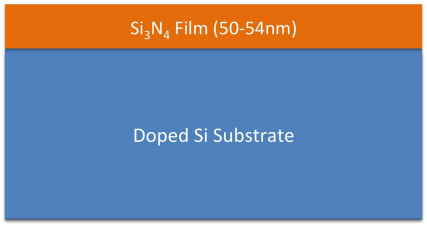

(b) Si_3N_4 film grown via chemical vapor deposition (CVD).

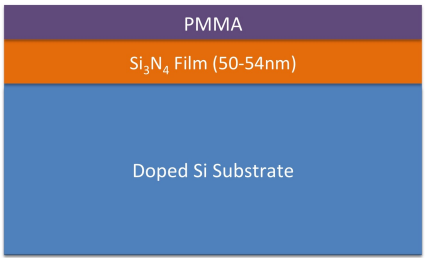

(c) PMMA applied via spin coat.

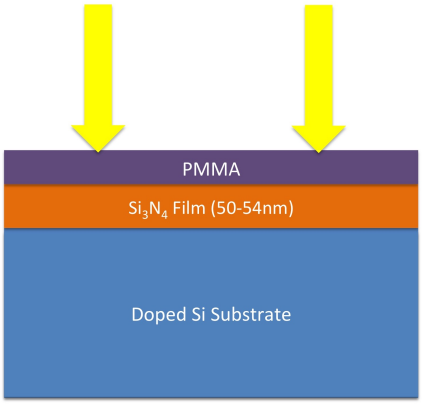

(d) Electron beam exposure.

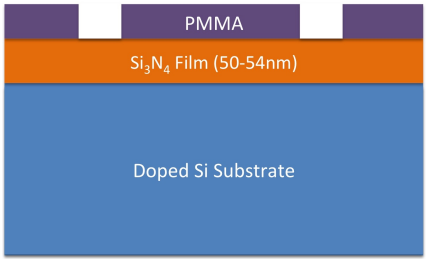

(e) Development.

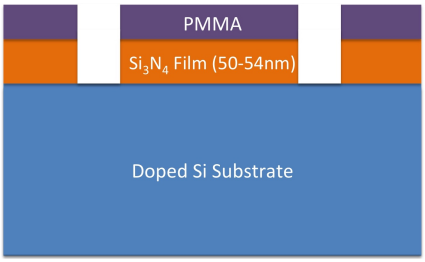

(f) Etching.

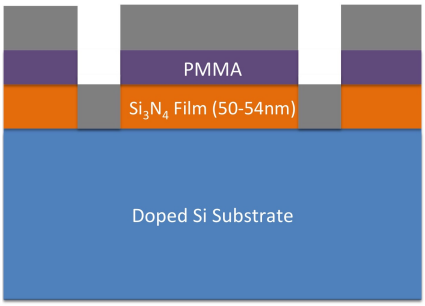

(g) Metal Deposition (or PMMA removal and measurement) .

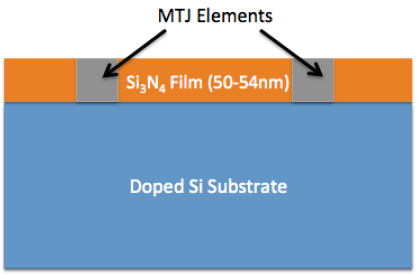

(h) Liftoff, leaving embedded elements.

Figure 5: Our basic embedded nanomagnet or MTJ fabrication process.

A summary of each of the processes needed to make most of the different types of samples studied in this thesis is given in the figure 6. The text that follows the figure describes each of these processes in detail. A summarized version of both is given in the appendix, for convenient reference.

Note that the actual embedded MTJ samples will be made in accordance with the "Patterned Sample (for Etching and Deposition)" method, but using a sputtered MTJ stack instead of metal deposited via electron beam evaporation and likely with a few other tweaks (discussed in sections 5.2.4, 5.4 and 6). A "PMMA Drop Sample" is used only for measuring the etch depth, roughness and sometimes anisotropy of a given RIE recipe. The "Patterned Sample (for Etching and Measurement)" is a sacrificial sample, used to determine the size, shape and depth of the holes on a "Patterned Sample (for Etching and Deposition)" after the two samples are etched simultaneously. These hole characteristics are nearly identical for two samples that are prepared and etched together using the same method (based on several experiments I ran to confirm this correlation). Thus, by taking measurements of the holes on the "Patterned Sample (for Etching and Measurement)", I can determine the depth, shape and size of the holes on the "Patterned Sample (for Etching and Deposition)" without removing its PMMA (which would ruin it). Lastly, the "Patterned Sample (for deposition)" fabrication procedure is the traditional nanolithography method used in our lab. I made a few nanodots this way to compare the shapes of nanodots made with sputtering vs. electron beam evaporation (our traditional nanolithography method). In addition, nanodots provide a somewhat simple way to test bilayer resist recipes (discussed in sections 5.2.4, 5.4 and 6).

PMMA Drop Sample	Patterned Sample (for etching and Measurement)	Patterned Sample (for etching and Deposition)	Patterned Sample (for deposition)
Prepare substrate	Prepare substrate	Prepare substrate	Prepare substrate
O_2 Clean, Descum	O_2 Clean, Descum	O_2 Clean, Descum	O_2 Clean, Descum
Apply PMMA Drop	Spin Coat	Spin Coat	Spin Coat
	Pattern	Pattern	Pattern
	Develop	Develop	Develop
Immediately before etch: O_2 Clean, Descum, O_2 Clean	Immediately before etch: O_2 Clean, Descum, O_2 Clean	Immediately before etch: O_2 Clean, Descum, O_2 Clean	Descum
Etch	Etch	Etch	
Remove PMMA	Remove PMMA	Deposit Metal	Deposit Metal
		Liftoff	Liftoff
AFM	AFM, repeat process for multi-material arrays	AFM, repeat process for multi-material arrays	AFM, repeat process for multi-material arrays

Figure 6: An overview of many of the fabrication processes used to produce the samples examined in this thesis. Descriptions of the individual steps are given below.

Prepare Sample:

1. Set hot plate to 180°C
2. Cut samples with diamond scratch.
3. Sonicate for 3 minutes in acetone.
4. Repeat step 3 with new acetone, then with IPA.
5. Rinse with deionized H_2O, dry with N_2.

6. Dry on hotplate at 180^{o}C for 1 minute.

Apply PMMA Drop:

1. Put PMMA drop on part of sample (use clean tweezers to minimize drop size).
2. Let cure for at least 1 hour (check that PMMA is dry).
3. Put samples on hotplate at 180^{o}C for 1 minute.
4. Let samples cool for at least 1 hour.

Etch:

1. Warm up/clean RIE using warm up recipe for the desired etching gas.
2. Check plasma (presence and consistency), reflected power, gas flows and pressure (though this may differ from the value when a sample is in the RIE).
3. Etch samples.
4. For each new gas, do O_2 clean, repeat previous etch steps.

Remove PMMA:

1. Acetone soak for at least 30 minutes, sonicate for 3 minutes in same acetone.
2. Repeat step 1 with new acetone.
3. Sonicate for 3 minutes in IPA.
4. Rinse with deionized H_2O, dry with N_2.

Spin Coat:

1. Set hot plate to 180^{o}C
2. Line bed of spin coater with paper towel.
3. Select Recipe 8.
4. Put sample on vacuum chuck, test vacuum by starting recipe and letting it reach maximum speed. Secure larger samples to vacuum chuck with double sided tape.
5. Discard first PMMA drop, then apply PMMA to sample until surface is almost covered.
6. Run recipe.
7. Bake on hotplate at 180^{o}C for 1 minute.
8. Scratch sample (start in center), add a cross scratch and corner scratches.

Develop:

1. Swirl in 3:7 H_2O: IPA for 1 minute.
2. Rinse with deionized H_2O, dry with N_2.

Liftoff:

1. Sonicate for 3 minutes in acetone.
2. Soak in new acetone for several hours (or overnight)

3. Sonicate for 3 minutes in new acetone.

4. Sonicate for 3 minutes in IPA.

5. Rinse with deionized H_2O, dry with N_2.

4.2 Reactive Ion Etching for Embedded Nanomagnet Fabrication

Reactive ion etchers, like the Technics 800 Series Micro-RIE I worked with, are typically used for etching to depths of over a micron. However, I had to make holes that were on the order of 50nm deep (roughly equal to the thickness of the Si_3N_4 film). In addition, I needed the etch depth to be predictable and repeatable. Lastly, the hole had to have high anistropy (cylindrical, not conical), in order to make good electrical contact with the doped substrate below the Si_3N_4. Since this is not commonly done, I experimented with new etching recipes to find one that would satisfy all of my requirements as best as possible.

Ideally, the bottom of the holes would be relatively smooth, in order to allow the deposited MTJ stack to perform as intended. However, there were potential solutions to high roughness (discussed in section 5.4), so this was of lesser concern initially. In fact, I determined the anisotropy would also not be a top priority, as long as the hole was not completely closed at the bottom. Thus, the most important goal was to find an etch that could give a predictable depth on the order of 50nm in Si_3N_4.

5 Results and Analysis

5.1 SF_6 Etching

I started my search for a suitable etching recipe with low power (30-70W) and using only SF_6 (with a 15 sccm flow rate). Most of these recipes produced decently linear depth vs. time results, on a given day. However, the depths for the same power and time varied quite significantly (often more than 100% difference) from day to day. Accurately predicting the depth of an etch is crucial to embedded nanodevice fabrication, so I concluded that none of these recipes would work for my purposes.

I hypothesized that the low power was creating an unstable plasma, which could sometimes be observed as flickering. This could cause somewhat random variations in the number and energy of ions hitting the sample, thus changing the etch rate, potentially accounting for the unrepeatable results. A potential solution to this problem is to raise the power.

I found that higher power (100-250W) SF_6 recipes produced surfaces with roughnesses up to 5 nm. Although there are methods for reducing roughness after etching, the roughness in this case was so significant that it often changed the depth (as measured by the AFM) somewhat randomly, again producing unpredictable results.

I looked for a "Goldilocks" zone between the roughness that came with higher powers and the flickering plasma that came with lower powers, but one did not exist. Thus, I had to find an alternative solution.

From other groups who were attempting to do somewhat similar things (though most of them were still etching to larger depths), I found that potential solutions to

my problem were to add oxygen [14] and/or substitute CF_4 for SF_6 [15], change the pressure, or add argon [16].

I could not add argon because our RIE did not have enough mass flow regulators. In addition, many of the lower pressures suggested by other groups for pure SF_6 etching were difficult to achieve or gave inconsistent (or no) plasmas in our RIE. Thus, the only potentially viable solutions were to try switching gasses and/or flow rates and their accompanying pressures.

5.2 SF_6 and O_2 Etching

5.2.1 Preliminary Recipes

For etching with SF_6 and O_2, I tried many combinations of power, flow rates (which determine the pressure) and gas ratio (O_2 flow rate/SF_6 flow rate). A summary of the different recipes I tried, along with a preliminary assessment of their potential viability based on the appearance of the plasma, is given in figures 7 and 8. Figure 7 is an overview of all the recipes, and the figure 8 is a zoomed in version, to better show some of the more successful recipes. Note that these figures also include the SF_6 only recipes discussed in the previous section, which have a gas ratio of 0.

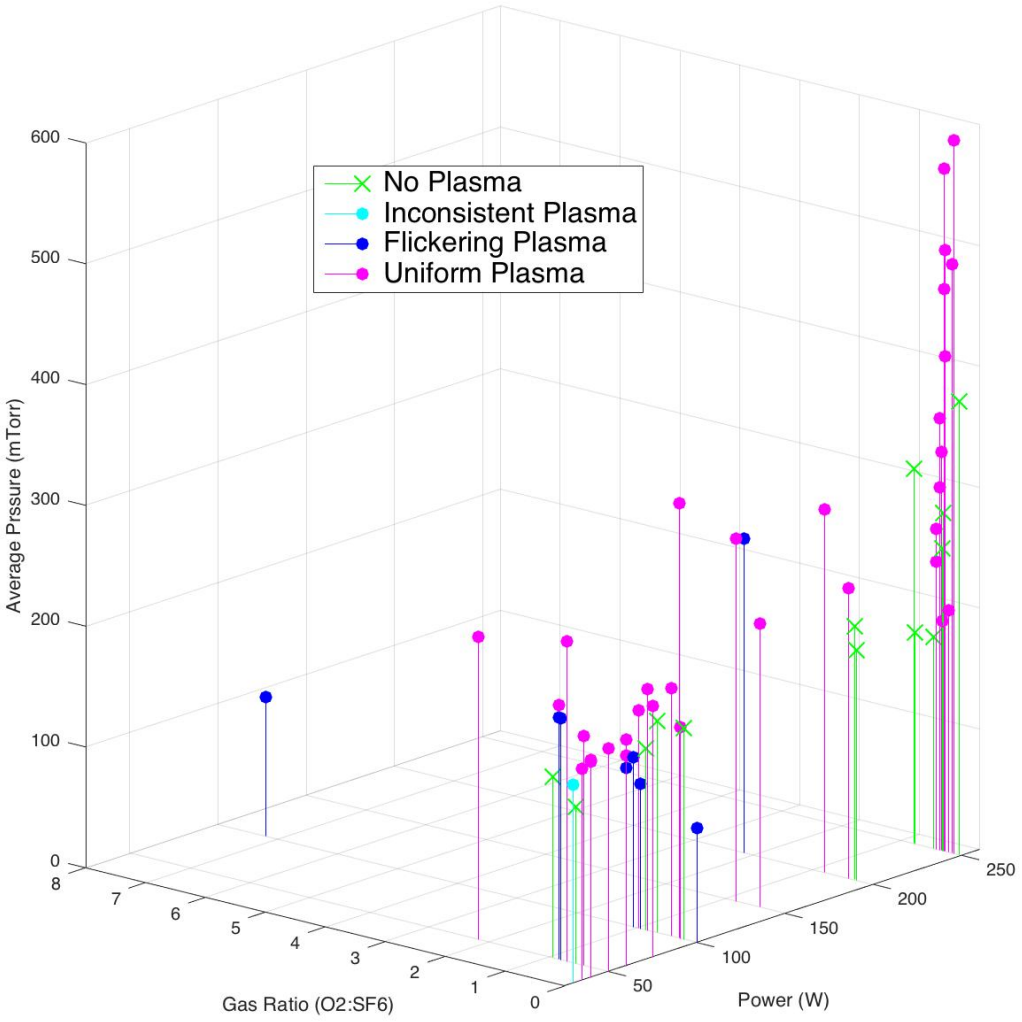

Figure 7: An overview of all the different recipes I tried for combinations of SF_6 and O_2.

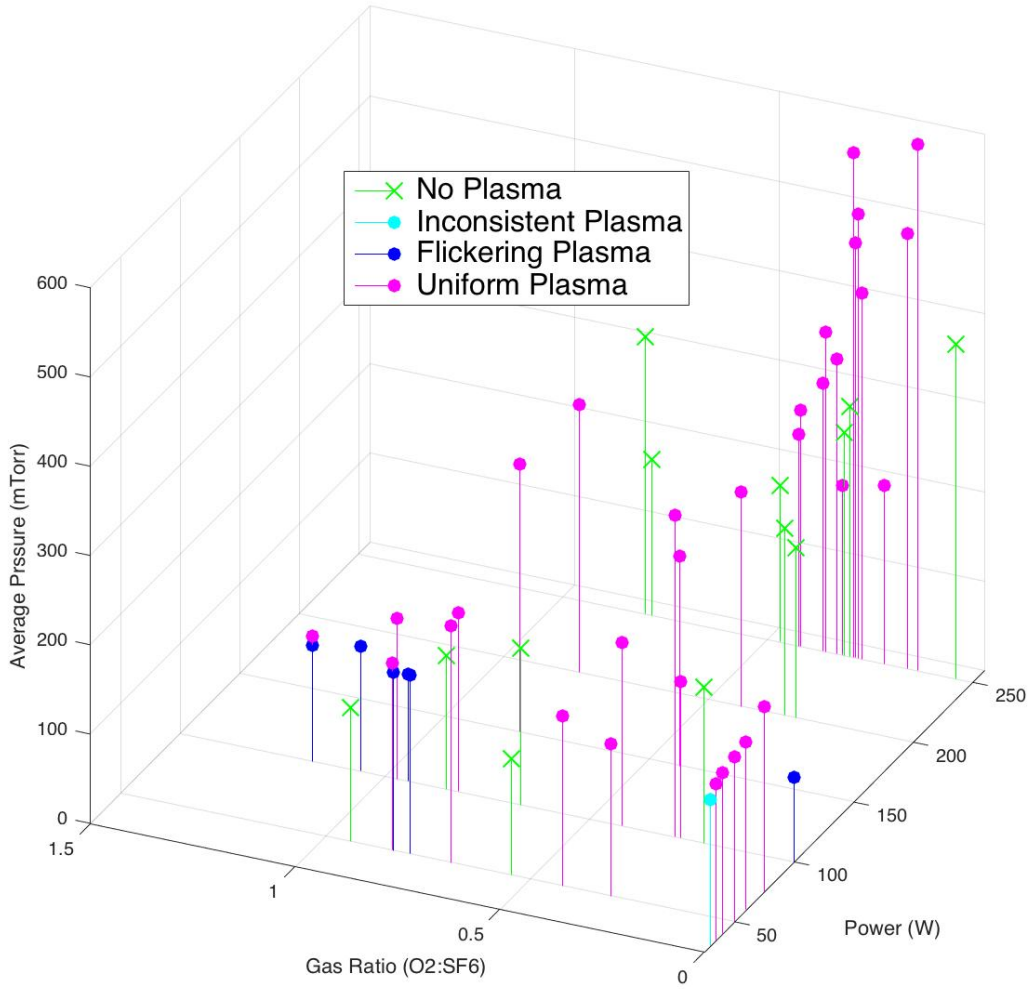

Figure 8: A closer look at some of the different recipes I tried for combinations of SF_6 and O_2 (zoomed in version of Fig. 7).

Even with the addition of O_2, lower power recipes still tended to produce flickering/inconsistent plasmas or unrepeatable results. Thus, I focused on higher power recipes, leading to the development of recipes 15, 18 and 21 (numbered in reverse order of creation for somewhat historical reasons).

Recipe 21 had a power of 200W, an SF_6 nominal/actual flow rate of 8/8.6 sccm and an O_2 nominal/actual flow rate of 1.5/3.6 sccm. Preliminary results for recipe 21 can be seen in figure 9. Note that in figure 9 and the other depth vs. time plots, the uncertainties on the depths are generally in the range of 1-2nm (unless otherwise stated) and are thus too small to be depicted visibly in these graphs.

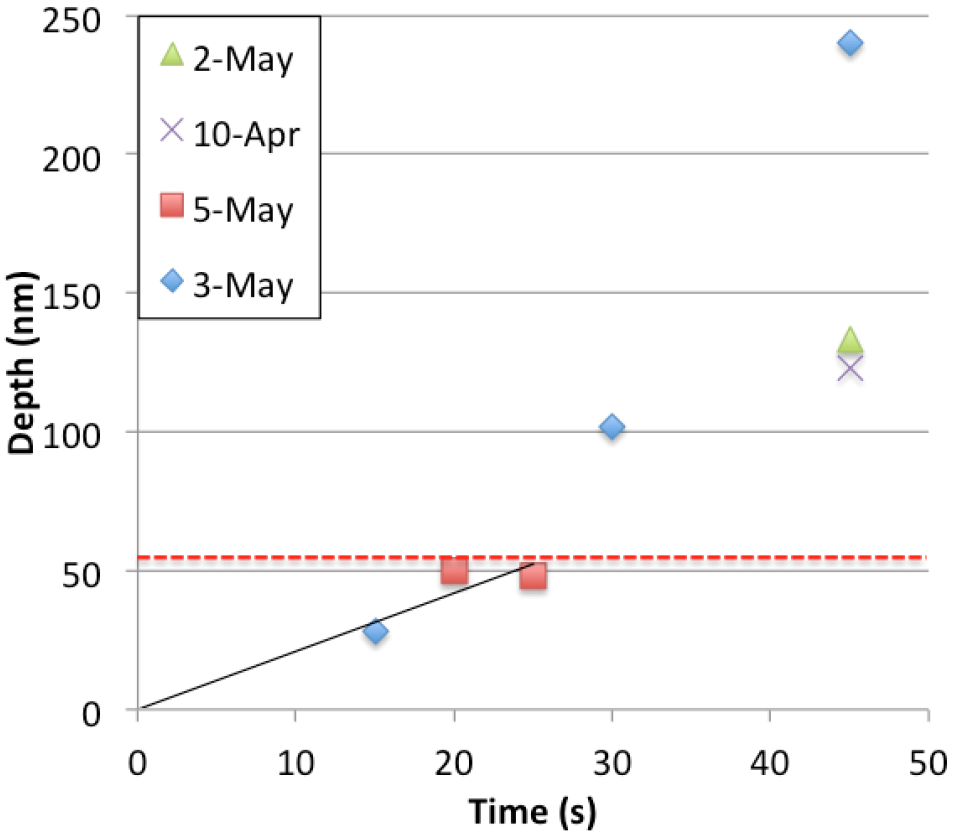

Figure 9: Depth vs. time for etches of PMMA drop samples done on different days with recipe 21. The horizontal dashed red line shows the depth of the Si_3N_4 film (54 nm here). The black line is a fit of the data points whose depths do not exceed that of the Si_3N_4 film. From this line, I calculated a Si_3N_4 etch rate of 2.1 nm/s.

The anistropy of the recipe 21's etch profile was low, which severely limited the minimum feature size that it would be able to produce on a patterned sample. In addition, the etch depth was not very repeatable, especially at higher depths. Thus, I determined recipe 21 was not a viable candidate for embedded nanomagnet fabrication.

Many of the aforementioned sources (particularly [14] and [16]) seemed to indicate

that changing the power could lead to better anisotropy for SF_6 and O_2 recipes. Since reducing the power seemed to give inconsistent plasmas, I raised the power to our RIE's maximum, 250W, leading to the development of recipes 18 and 15.

Recipe 18 had a power 250W, an SF_6 nominal/actual flow rate of 16/16.4 sccm and an O_2 nominal/actual flow rate of 2/3.6 sccm. The preliminary etch depth results can be seen in figure 10.

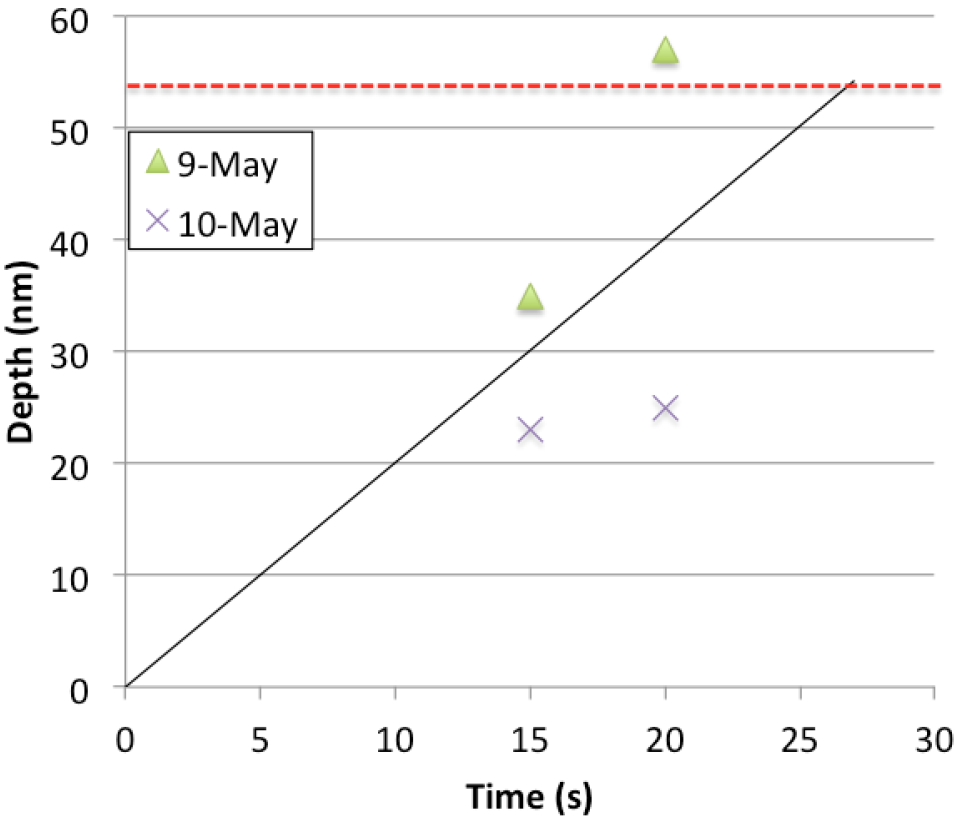

Figure 10: Depth vs. Time for etches of PMMA drop samples done on different days with recipe 18. The horizontal dashed red line shows the depth of the Si_3N_4 film (54 nm here). The black line is a fit of the data points whose depths do not exceed that of the Si_3N_4 film. From this line, I calculated a Si_3N_4 etch rate of 2.0 nm/s.

The anisotropy improved significantly from recipe 21 to recipe 18, but the etch depth was again not very repeatable, as seen in figure 10.

5.2.2 Recipe 15

Unfortunately, very few papers that discuss etch depth repeatability on the nanometer scale have been published. However, many papers on Si_3N_4 etching (to greater depths, generally), such as [14], suggest increasing oxygen flow to create a passivization layer in an attempt to increase anisotropy. I hypothesized that this might also have a positive effect on the repeatability of the etch depth by preventing the etchant ions from making contact with the sidewall and thus reducing unpredictable changes in etch rate due to horizontal etching.

With this theory in mind, I increased the oxygen flow in recipe 18, leading to recipe 15 which had a power of 250W, an SF_6 nominal/actual flow rate of 16/16.4 sccm and an O_2 nominal/actual flow rate of 4/6 sccm. Etch depth vs. time data for recipe 15 from several different dates can be seen in figure 11.

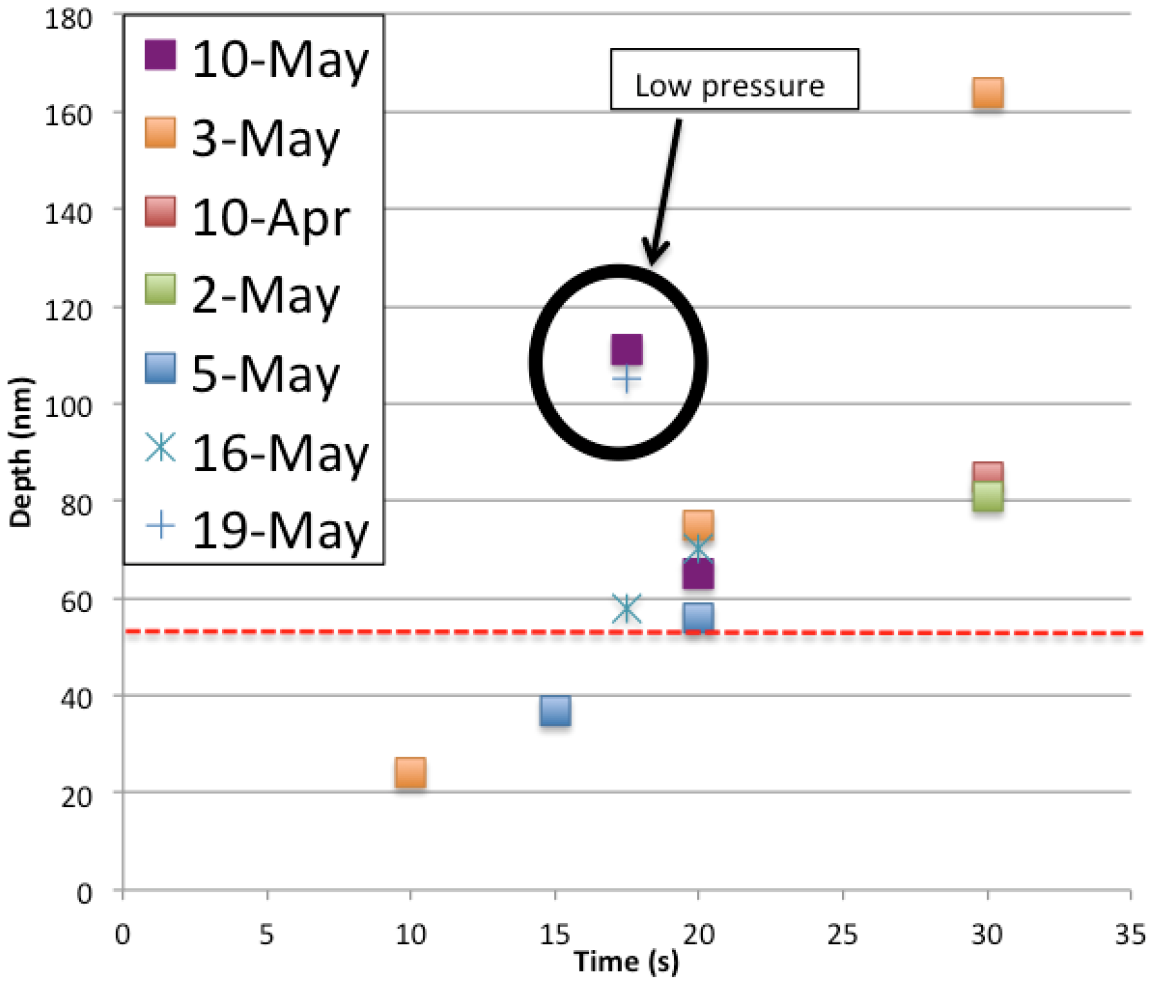

Figure 11: Depth vs. time for etches of PMMA drop samples done with recipe 15 on different days. The horizontal dashed red line shows the depth of the Si_3N_4 film (54 nm here)

Generally, the depth of etches done with recipe 15 for 17.5-20 seconds was fairly repeatable. It tended to reach depths slightly greater than the thickness of the Si_3N_4 (54 nm: shown by horizontal red line in figure 11), as desired for embedded

MTJ/nanomagnet fabrication. However, the trend was occasionally interrupted by unexpectedly low pressures during etching. These seemed to occur randomly and lasted for the duration of an etch. When they did occur, the etch rate increased significantly, thus producing a greater depth for the same etch time.

The correlation between low pressure and high etch rate is consistent with Bernoulli's principle. A lower pressure leads to higher average particle velocities, which causes them to impact the substrate with higher kinetic energies, thus increasing the probability of material removal via sputtering and ultimately increasing the etch rate.

This theory can be further confirmed by examining the anisotropy. Generally, an increase in the amount of material removed by sputtering leads to a steeper slope along the etched/unetched interface, because sputtering is a more anisotropic process than other RIE material removal mechanisms. Comparing the slopes of the samples that experienced low pressures during etching to those that did not (but were etched for longer times to achieve somewhat comparable depths), I found a correlation between low pressure and high anisotropy. For example, sample 70 was etched for 17.5 s on May 19th using recipe 15, with an average pressure of 275 mTorr. I found that it had an etch depth of 105 nm and an interface slope of 0.11. For comparison, sample 55 is fairly representative of the "normal pressure" samples. It was etched for 30 seconds on May 3rd using recipe 15, with an average pressure of 300 mTorr. This led to an etch depth of 164 nm and an interface slope of 0.078. Thus, it is quite likely that low pressure leads to an increase in particle velocity via Bernoulli's principle, allowing for an increase in sputtering and thus a greater etch depth and higher anisotropy.

While the seemingly randomly occurring higher etch rates in recipe 15 are detectable (via the pressure readout), I could not find a reliable way of preventing them. However, an etch depth that was greater than intended could potentially be corrected by backfilling with metal, as long as the depth was known. Thus, I proceeded to use recipe 15 to etch a nanopatterned sample, since recipe 15 gave the most repeatable and anisotropic etching results of any SF_6 and O_2 recipe. An example of one of the holes etched this way can bee seen in figure 12.

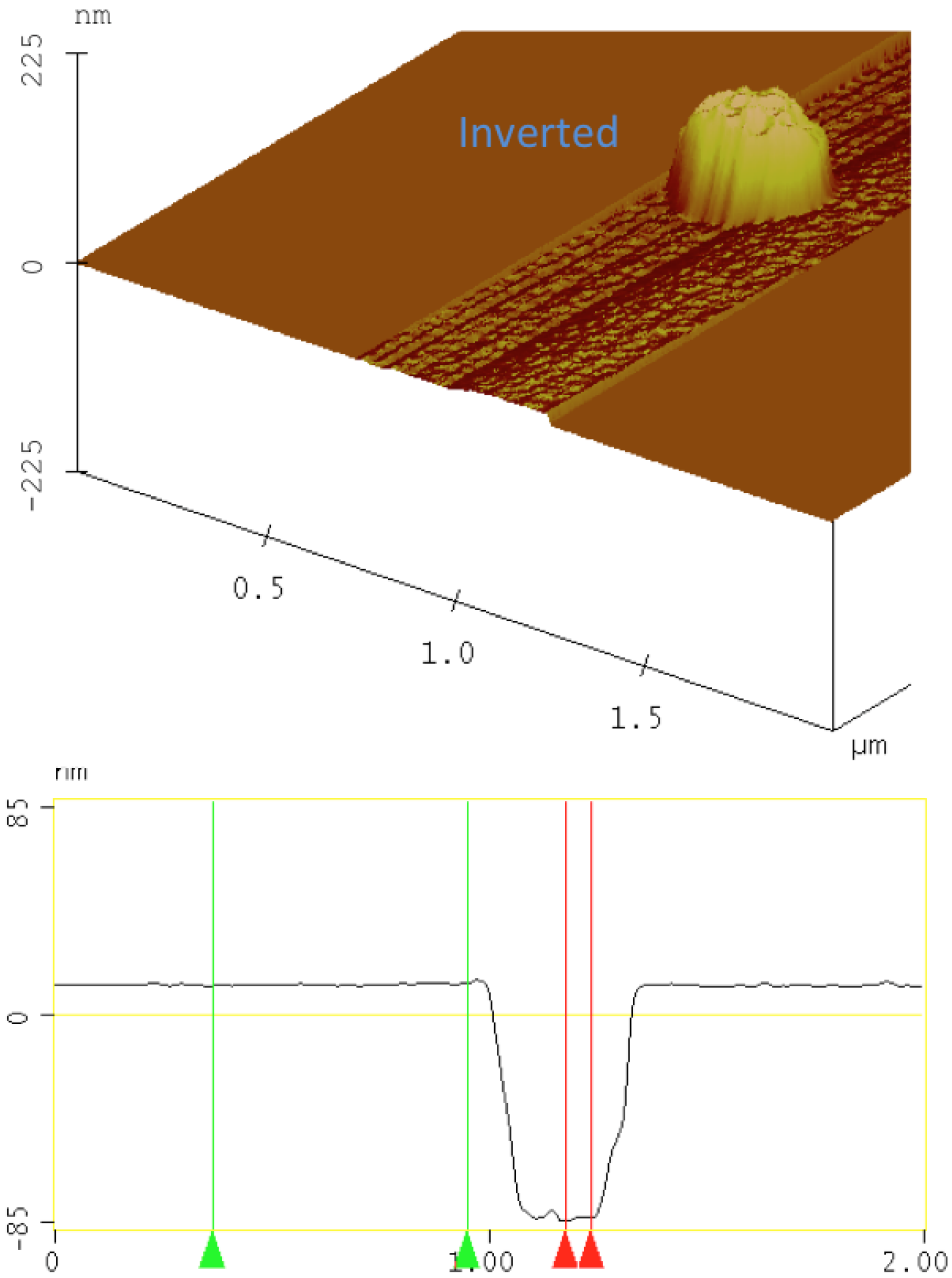

Figure 12: An inverted 3D AFM image (top) and an AFM cross section (bottom) of a hole etched in a patterned sample using recipe 15. The hole has an approximate diameter and depth of ∼300 nm and ∼95 nm, respectively.

The anisotropy and roughness of the hole shown in figure 12 are similar to those of the holes of other diameters from the same sample. However, the depth decreases slightly from the nominal (PMMA drop) depth with diameter, as seen in figure 13.

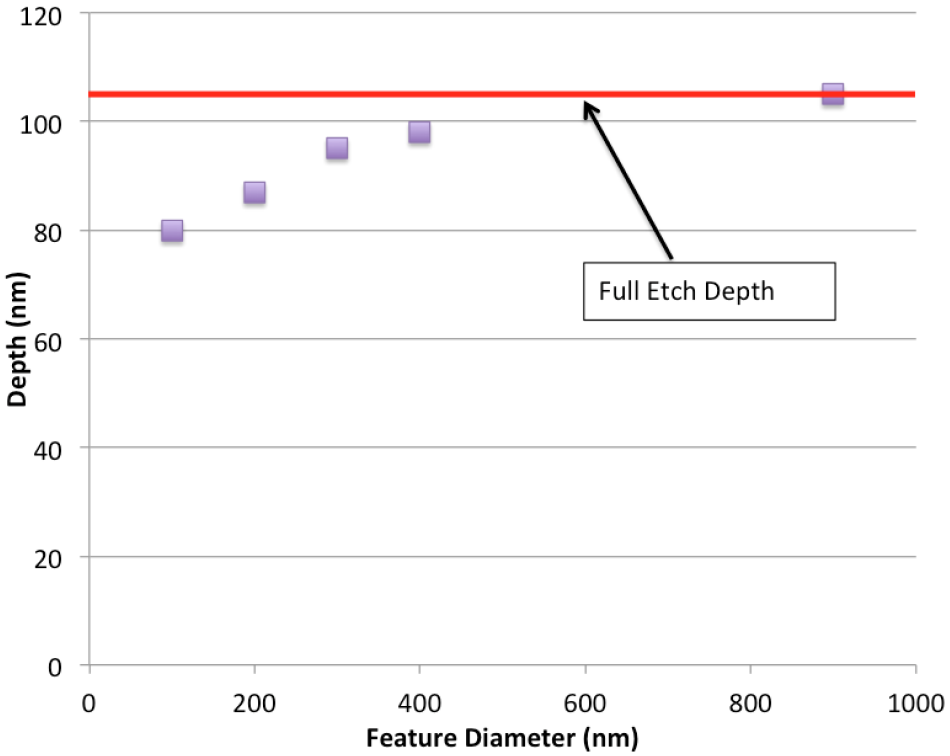

Figure 13: Etch depth vs. feature diameter for a patterned sample etched with recipe 15. The red line represents the full etch depth, determined from a PMMA drop sample that was etched with the patterned sample.

Seemingly by coincidence, the pressure during this particular etch was low. As expected from Figure 11, this led to an increased etch depth (∼100 nm instead of ∼50 nm for a 17.5 s etch.). Additionally, it likely led to a slightly increased anisotropy, as explained earlier in this section. However, when the anisotropy of these holes was measured, it was found to be much higher than the comparable etches performed

on PMMA drop samples (interface slopes in the range of 0.5 to 0.9 instead of 0.05 to 0.1). This change can be attributed in part to the inability of the AFM tip to accurately record the profile of the hole, because its diameter is relatively small, compared to its depth. However, it is also likely that there is a significant difference between the anisotropy created by an etch performed at the edge of a PMMA drop and a comparable etch done in the center of a spin coat-applied PMMA film that has been patterned. Another manifestation of this difference can been seen in the "dip" samples created with recipe 37 that are discussed in section 5.3.2.

5.2.3 Incremental Etching

As mentioned previously, etching to a depth beyond the thickness of the Si_3N_4 film could potentially be corrected by backfilling. However, too much backfilling would likely lead to an undesirable profile. Thus, I began to use "incremental etching" in an attempt to achieve a depth closer to the film thickness.

Incremental etching is essentially just a series of shallow etches. After each etch, the total depth of the real sample is determined by measuring the depth of sacrificial samples that are etched with the real one. This has the potential to give a final depth closer to the desired depth, but it comes at the price of a large uncertainty on the total depth, profile and roughness.

5.2.4 First Etched MTJ Sample

Using the incremental etching method and recipe 15, I made my first etched MTJ sample. It required two etches because the first etch was only ∼31 nm, giving a total

depth of 66 +/- 15 nm. The relatively large uncertainty on the final depth is due to the nature of the incremental etching method, as discussed in the previous section.

After I had etched it, BYU sputtered an MTJ stack onto the sample with a composition of Substrate/Ta(40)/CoFeBe(1.25)/MgO(0.9)/CoFeB(1.4)/Ta(4), for a total thickness of approximately 48 nm. Thus, the net result should have been a flat MTJ stack embedded in the etched hole extending to a height of somewhere between 3 and 33 nm (based on the uncertainty on the total etch depth) below the substrate surface. However, the actual result was much less uniform than expected.

Images of a 500nm diameter hole that is fairly representative of all the holes (300nm, 400nm, 500nm) on this sample after the etching and MTJ deposition can be seen in figure 14.

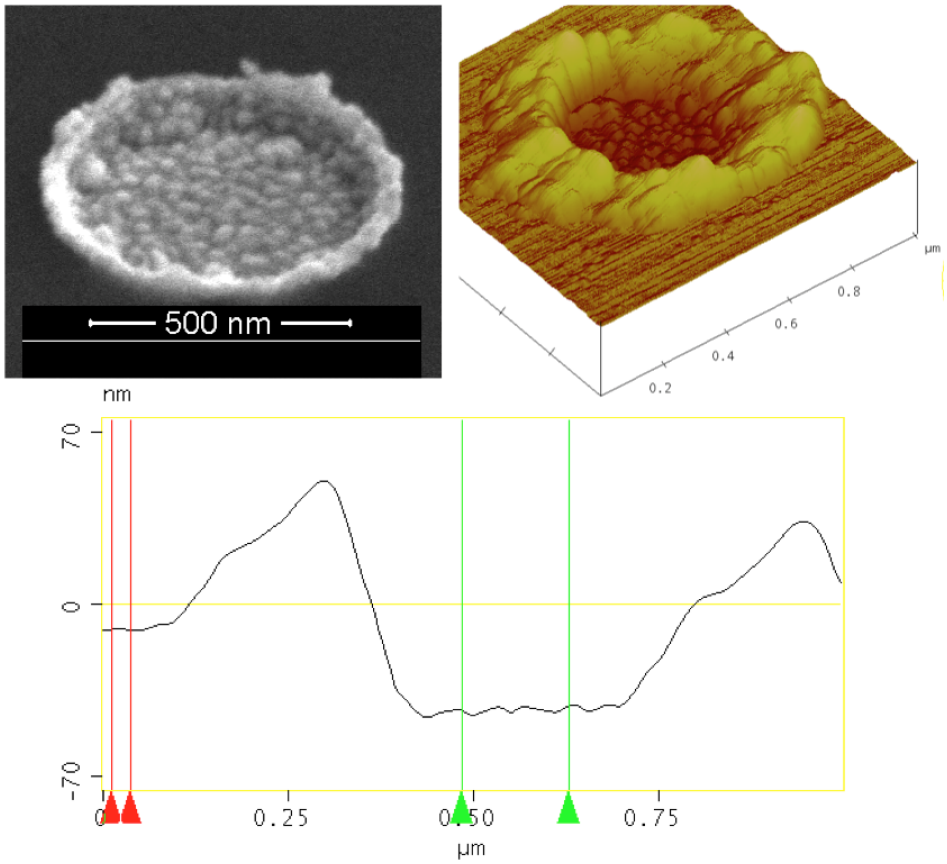

Figure 14: An SEM image (top left), 3D AFM image (top right) and an AFM cross sectional image (bottom) of a 500nm diameter hole from the the first etched MTJ sample, after it was etched and then filled with an MTJ stack.

All of the holes on this sample after MTJ deposition had the undesirable ring shape seen in figure 14. For the 500nm diameter hole, the center is ∼33 nm below the substrate and the outer ring is ∼60 nm above the substrate. Measurements were similar for the other holes.

For comparison purposes, the first etched MTJ sample also included nanodots that were fabricated without etching, using the standard Patterned Sample (for

deposition) EBL process. Figure 15 shows images of a 400nm diameter nanodot that was made on the same chip and of the same MTJ stack as the features shown in figure 14. Its shape is fairly representative of the other nanodots of varying size on this sample.

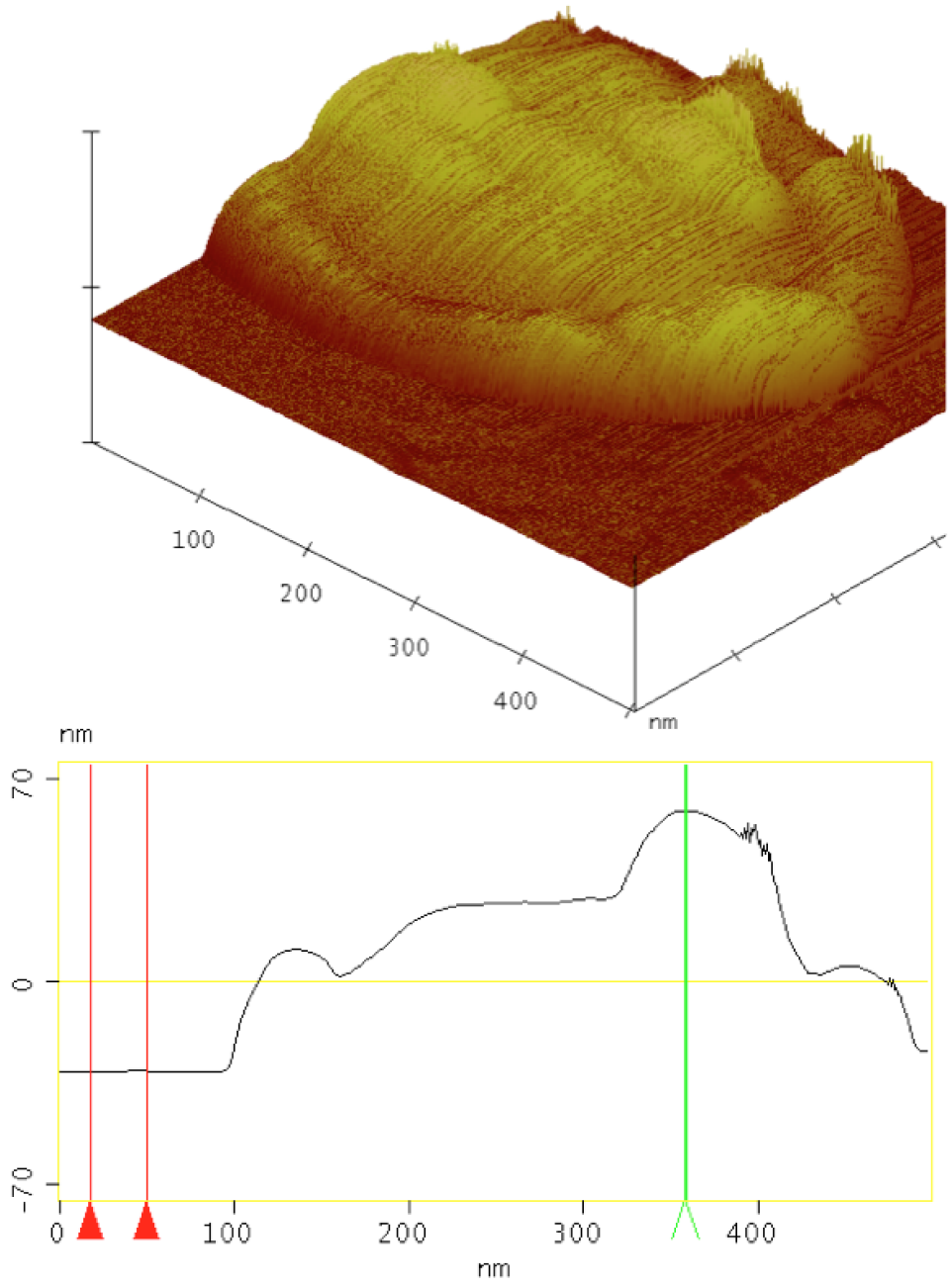

Figure 15: A 3D AFM image (top) and an AFM cross sectional image (bottom) of a 400nm nanodot (no etching) from the first MTJ sample. Note the deviation from a standard cylindrical profile.

Similar nanodots are commonly fabricated in our group and have a consistently cylindrical or slightly conical shape. However, the shape of the nanodots on this sample is clearly much worse.

The fact that both the embedded MTJ and the nanodot MTJ had unexpected shapes seems to indicate that the change in shape came from the deposition of the MTJ stack via sputtering, rather than from another step in the fabrication process. An explanation of why this might occur can be seen in figure 16.

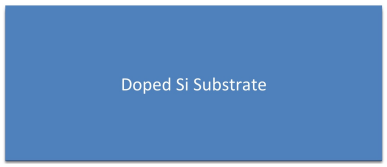

(a) Bare doped silicon substrate.

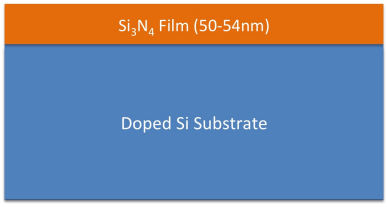

(b) Si_3N_4 film grown via chemical vapor deposition (CVD).

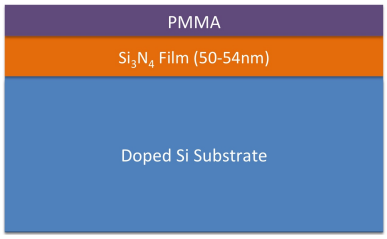

(c) PMMA applied via spin coat.

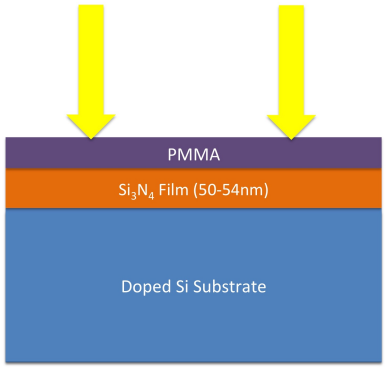

(d) Electron beam exposure.

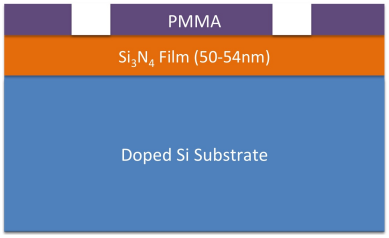

(e) Development.

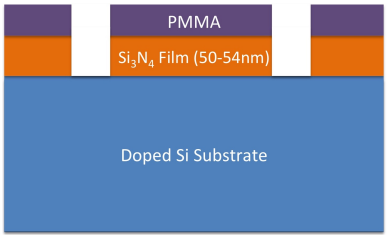

(f) Etching.

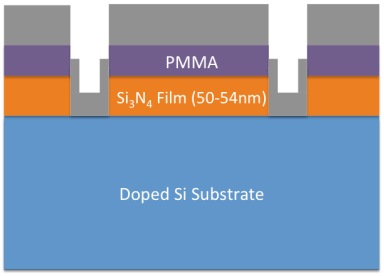

(g) MTJ stack deposited via sputtering. Notice that some of the metal now sticks to the sides of the holes, preventing some of it from landing below the surface of the Si_3N_4 and instead creating an outer ring.

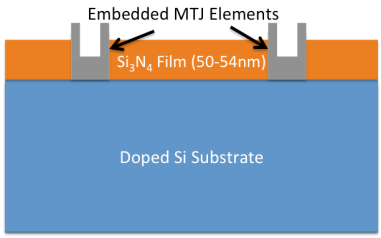

(h) Liftoff, leaving ring-shaped MTJ elements, which are unlikely to work for their intended purpose.

Figure 16: Our basic embedded MTJ fabrication process when sputtering is used to deposit the metal.

As seen in figure 16, it is likely that our standard nanopatterning procedure would produce ring-shaped nanodots on embedded MTJs when the MTJ material is deposited with sputtering (which is necessary to preserve the stoichiometry of the materials used). To test this theory, I used the single-layer resist etching process illustrated in figure 5 to make two samples, but I did the metal deposition with our e-beam evaporator, rather than a sputterer. They both showed nearly ideal profiles after metal deposition (no ring shape). More details on these samples can be found in section 5.3.3. This result indicates that sputtering was likely the primary cause of the odd shape seen in the first etched MTJ sample. However, the etch itself contributed to the depth uncertainty and possibly also the ring-shaped profile and high roughness.

A possible solution to the undesirable ring shape is to use a bilayer resist. The lower resist layer consists of something like MMA-MAA Copolymer or PMMA 495 (what I have been referring to as "PMMA" is PMMA 950). The important characteristic of the underlying resist layer is that it is more sensitive to the electron beam than is the upper layer, which consists of PMMA 950. The net result is that, after patterning and development, resist is removed from a larger area of the lower resist layer than from the upper layer. This should create an overhang of PMMA 950, making it harder for deposited metal to stick to the sidewalls and thus allowing it to fill the hole, as desired, while eliminating the undesirable ring shape that we observed on the first etched MTJ sample. This process is illustrated and detailed in figure 17.

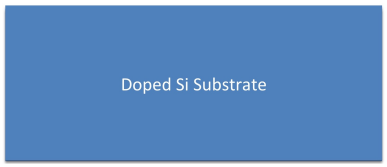

(a) Bare doped silicon substrate.

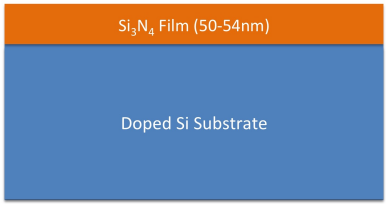

(b) Si_3N_4 film grown via chemical vapor deposition (CVD).

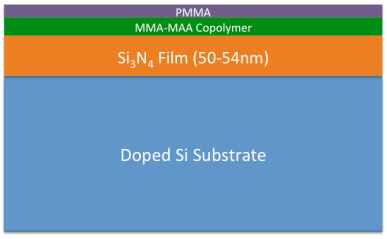

(c) Photoresists applied via spin coat. The MMA-MAA copolymer (or similar resist) is more sensitive to electron beam exposure than is the PMMA.

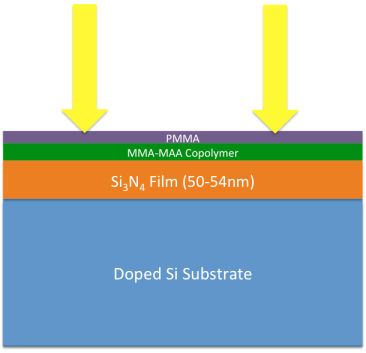

(d) Electron beam exposure.

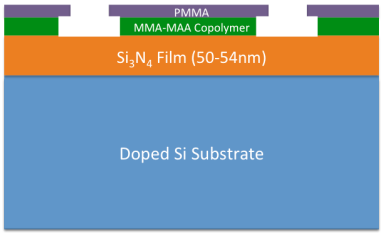

(e) Development.

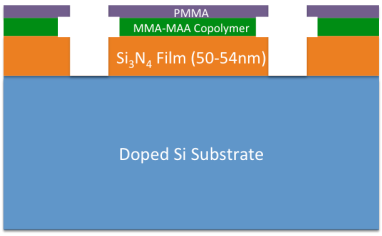

(f) Etching.

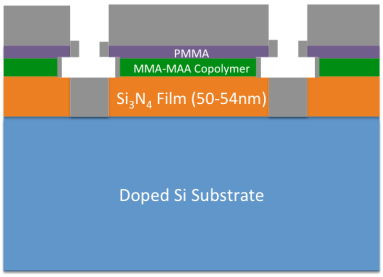

(g) MTJ stack deposited via sputtering.

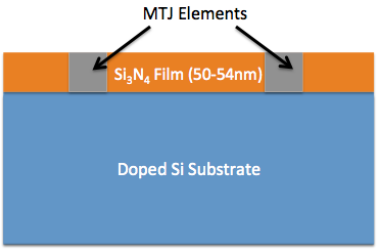

(h) Liftoff, leaving cylindrical embedded elements, as required for them to function as intended.

Figure 17: Our embedded MTJ fabrication process when sputtering is used to deposit the metal and a bilayer resist is applied.

Notice in Figure 17 (e) the increased photosensitivity of the copolymer causes the electron beam exposure/development steps to remove more of it than the PMMA, leaving a PMMA "overhang". Additionally, notice in Figure 17 (g) that less of the metal sticks to the sides, allowing more to fill the hole. The small amount of metal that does stick to the sides is not connected to the metal in the hole and can thus be removed easily during liftoff.

To fully develop and test the bilayer resist method may require a comprehensive study of more sensitive resists to act as the bottom layer. In addition, it is likely that we would need to experiment with different spin coating and drying methods, times and speeds to optimize the thicknesses of each layer and then change the electron beam doses to create features of the desired shape and size. This work is currently in progress, but it is difficult to test it thoroughly without regular access to a sputterer.

5.3 CF_4 and O_2 Etching

Recipe 15 gave the most repeatable results for SF_6 and O_2 etching. However, it still somewhat randomly gave significantly increased etch depths (correlated with low pressures). Even with incremental etching, recipe 15 still gave somewhat unpredictable depths with large uncertainties. It simply wouldn't produce the predictable depth needed for successful fabrication of embedded MTJs. Thus, I switched my etching gases to CF_4 and O_2, in an attempt to develop an etching recipe that gave more repeatable results.

5.3.1 Preliminary Recipes

I tried several combinations of parameters for CF_4 and O_2 etching, eliminating some recipes based on the visual appearance of the plasma, and others based on repeated studies of the etch depth and profile. Note that significantly fewer trial recipes were required for CF_4 than for SF_6 because many of general trends of the SF_6 recipes about what parameter combinations are likely to give desirable results transferred well to CF_4 recipes. An overview of the parameter space I covered for CF_4 and O_2 etching is given in figures 18 and 19.

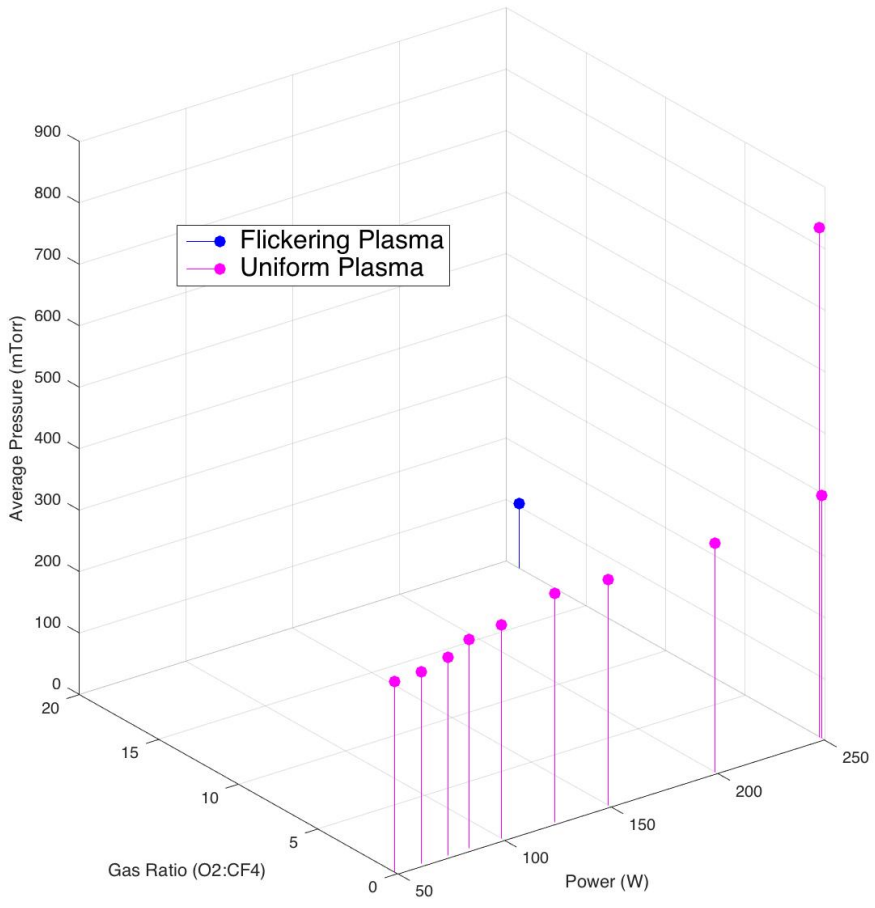

Figure 18: An overview of all the different recipes I tried for combinations of CF_4 and O_2.

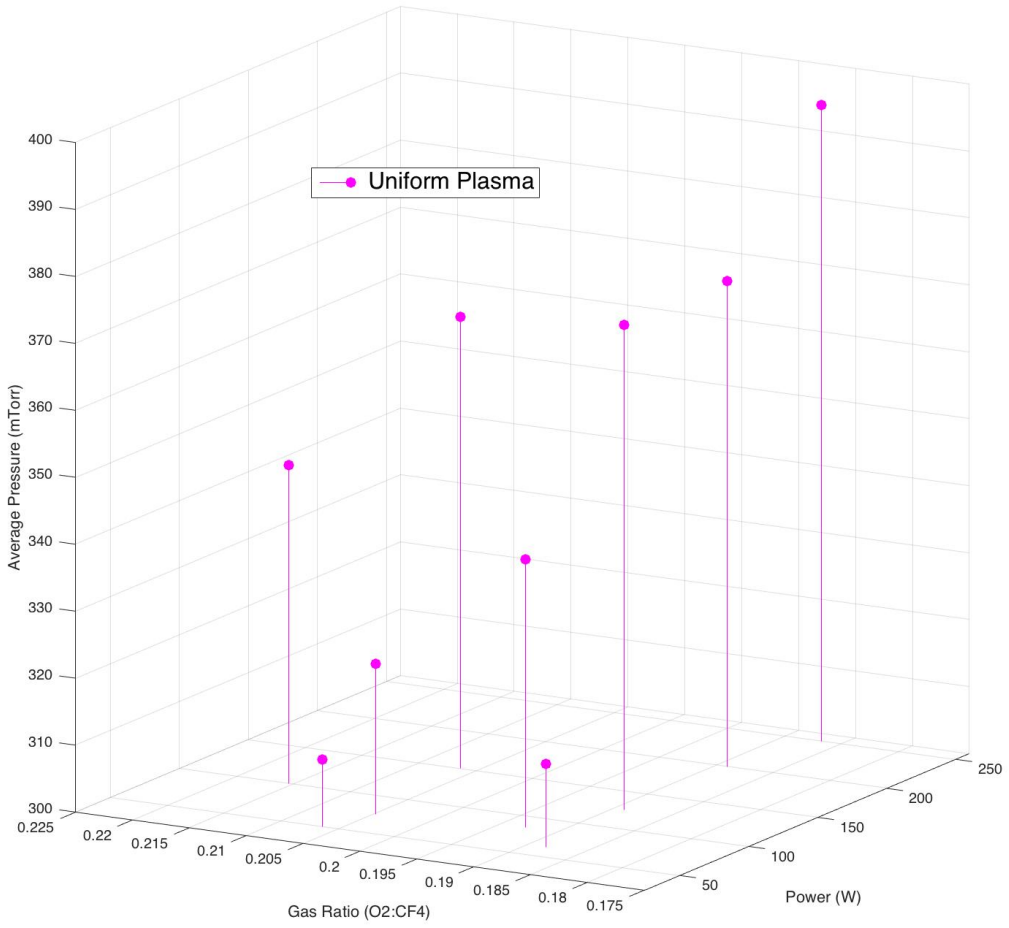

Figure 19: A closer look at some of the different recipes I tried for combinations of CF_4 and O_2 (zoomed in version of Fig. 18).

From these preliminary studies, I determined that recipes with a CF_4 nominal/actual flow rate of 25/25.4 sccm and an O_2 nominal/actual flow rate of 3.1/5.2

sccm produced the most promising results in terms of plasma consistency, which is almost certainly correlated with etch profile and repeatability. These flow rates are similar to those used by BYU [15].

Next, I studied the effect of power on the etch rate with the gas flow rates set to the values given above and the time fixed at 30 seconds. The results of this study are shown in figure 20.

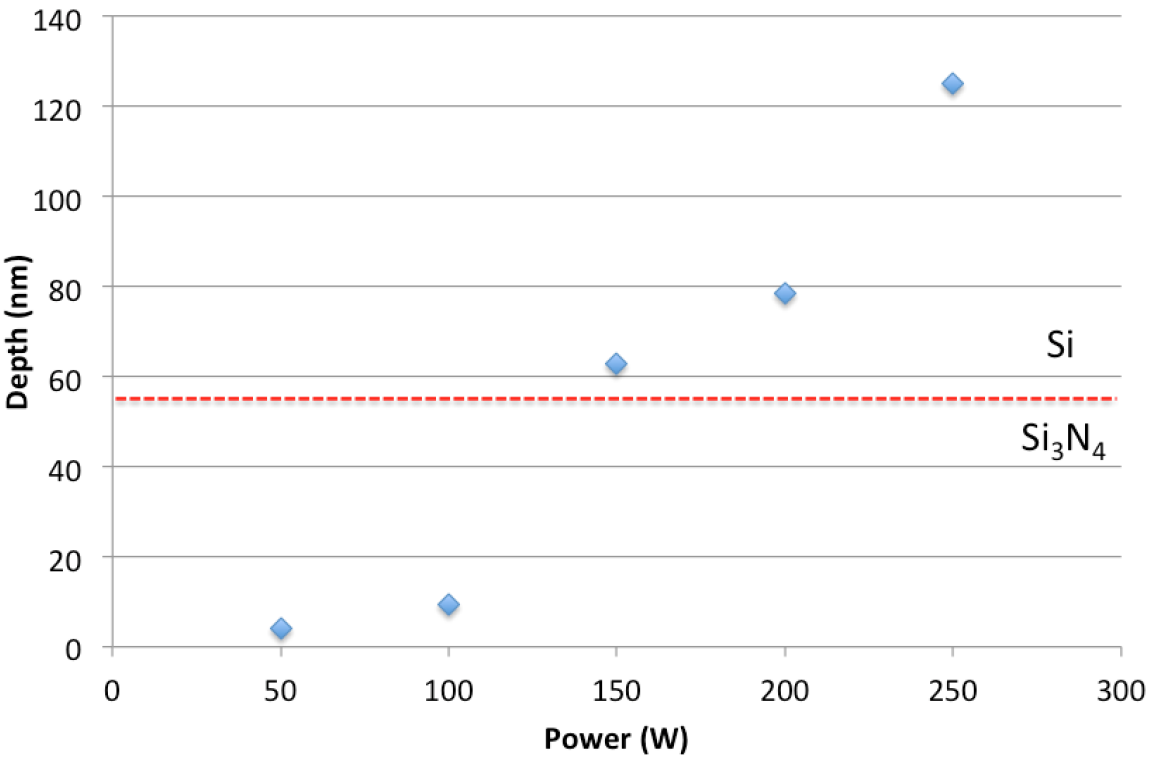

Figure 20: Depth vs. power for a 30 second etch with a CF_4 nominal/actual flow rate of 25/25.4 sccm and an O_2 nominal/actual flow rate of 3.1/5.2 sccm. The horizontal dashed red line shows the depth of the Si_3N_4 film (50 nm here).

As with SF_6 and O_2 etching, I found that lower powers give unrepeatable results. Specifically, most of the powers under 150W gave depths that differed from day to day by as much as 60nm for the same etch time. Thus, I focused on 150, 200, 250W. Ultimately, I again found that the highest power gave the most repeatable results.

5.3.2 Recipe 37

In general, recipe 37 (Power: 250W, CF_4 nominal/actual flow rate: 25/25.4 sccm, O_2 nominal/actual flow rate: 3.1/5.2 sccm) was the best recipe I developed in terms of repeatability and anisotropy. However, some samples had an unexpected profile, which included a significant dip at the edge between the etched and unetched surfaces. An example of such a sample can be seen in figure 21.

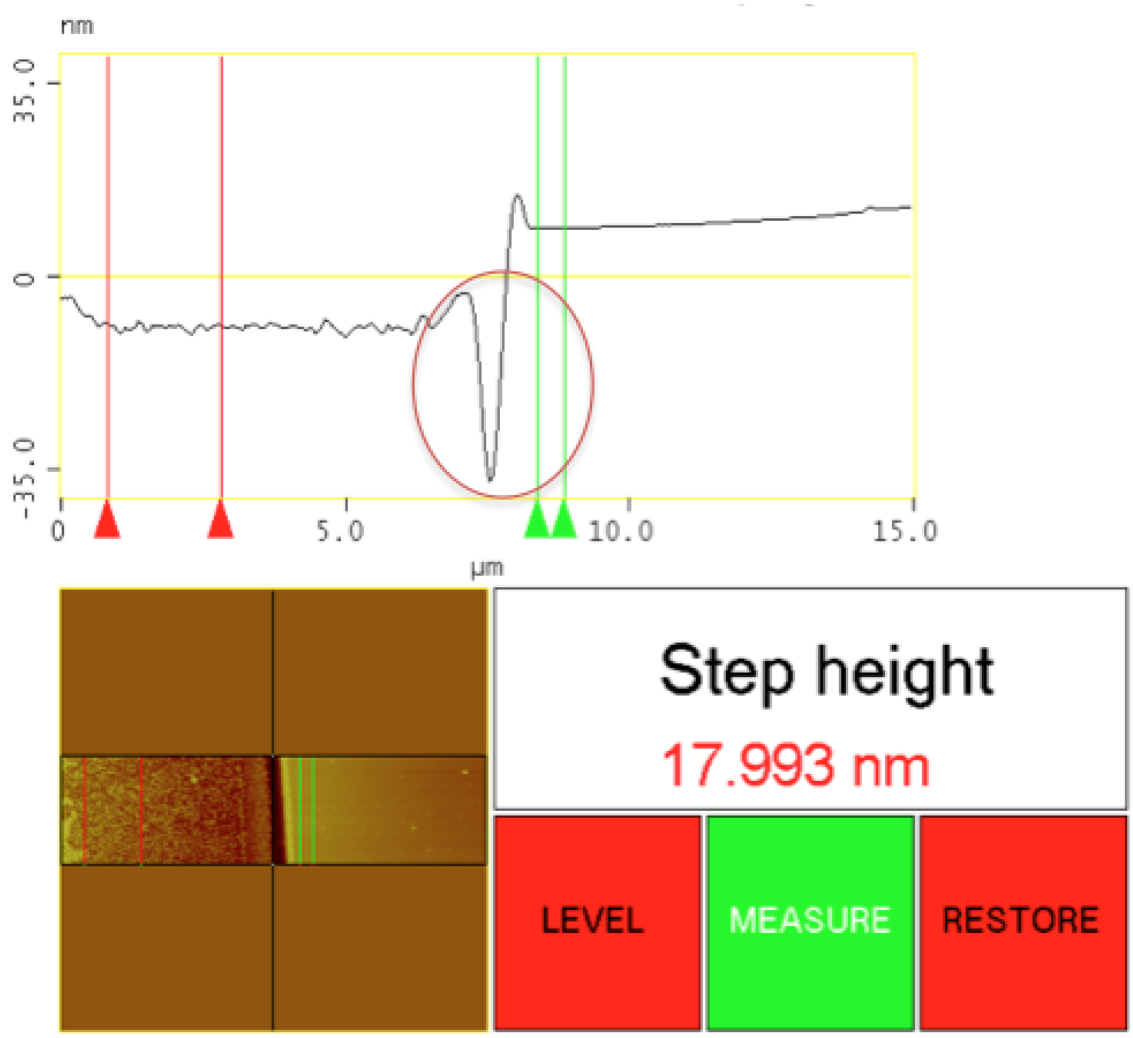

Figure 21: An example of a PMMA drop sample etched with recipe 37 that has the aforementioned dip.

This dip was not observed regularly in other recipes and its cause is not understood at this time. Samples that had this dip did not fit with the general trend of the rest of the depth vs. time data, as shown in figure 22.

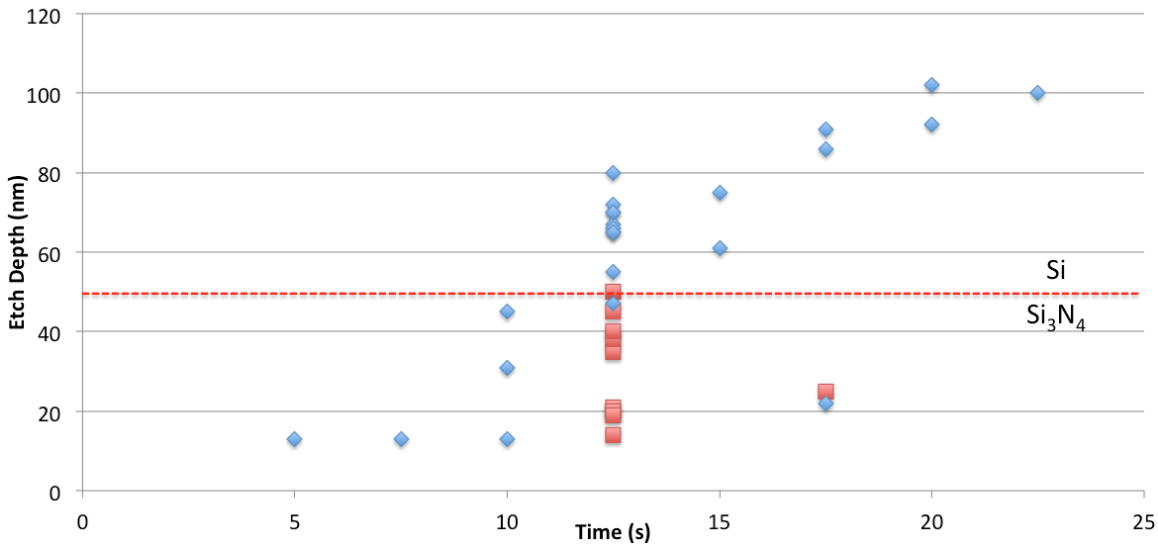

Figure 22: Depth vs. time for etches of PMMA drop samples done using recipe 37. Samples with the standard step-like profile are shown in blue, while those with a "dip profile", as described previously, are shown in red. The horizontal dashed red line shows the depth of the Si_3N_4 film (50 nm here).

Atypical PMMA drying may be a partial cause of the dips, but this alone would not explain the fact that I consistently observed these dips only on PMMA drop samples etched with recipe 37. However these dips should not be an issue on patterned samples because the holes are so small that they will likely be within the lateral range of the dips, allowing them to reach the full desired etch depth. Thus, I experimented with excluding the samples that had the dip profile from my depth vs. time data, the results of which can be seen in figure 23.

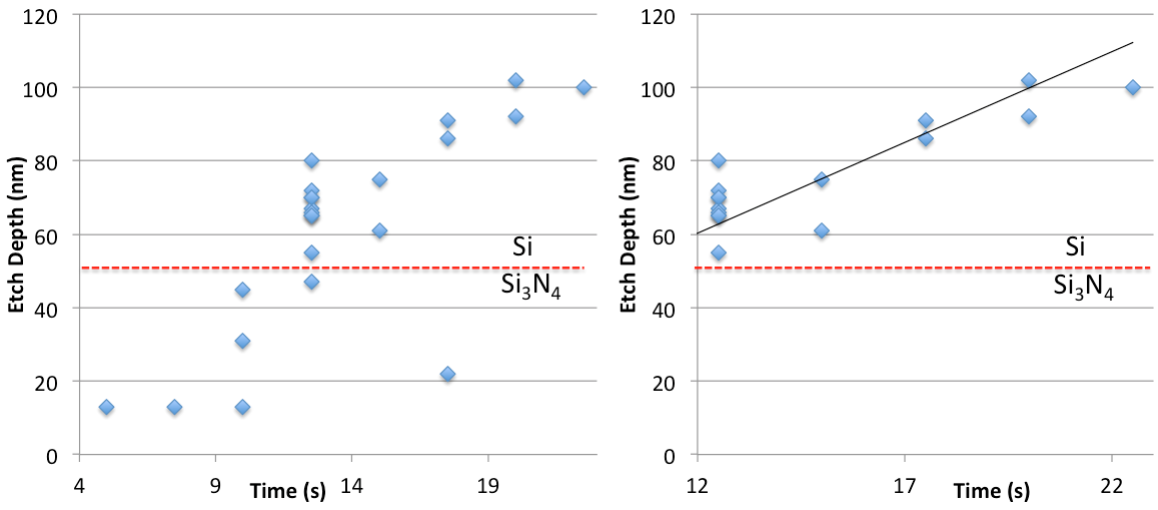

Figure 23: Left: Depth vs. time for etches of PMMA drop samples using recipe 37, with the "dip" samples removed. Right: Same as the left, except only etches that reached to or beyond the Si_3N_4/Si interface are shown. This material boundary is at a depth of 50 nm, as shown by the the horizontal dashed red line in both plots. The etch rate in Si, as determined from the fit of the data shown in the right plot, is 4.9 nm/s.

Once the samples with a dip are removed, the data becomes much more linear and the depths for a given time are much more consistent, particularly beyond 50 nm. If a patterned sample (rather than a PMMA drop) were etched with recipe 37, it is likely that the etched holes would have a depth similar to the bottom of the dip (which is difficult to measure on PMMA drop sample), because their diameter is typically smaller than the width of the dip. This indicates that recipe 37 would probably give consistent depth results when producing a real embedded MTJ sample. The results of tests of this theory are presented in the next section.

5.3.3 Embedded Nickel Nanomagnets

I patterned several samples to test my theory about the dips that appeared in the profiles of some PMMA drop samples etched with recipe 37. I then etched all of these samples at once; one for measurement (sample A57), one for backfilling (sample A58) and an extra two just in case I needed to implement the incremental etching method (if the etch was not deep enough). Some of the holes of different sizes that I measured on sample A57 can be seen in figure 24.

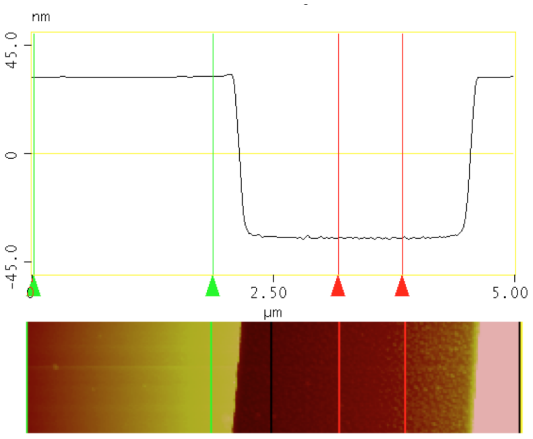

(a) A 2 um wide trench. The measured depth was 68 ± 2 nm.

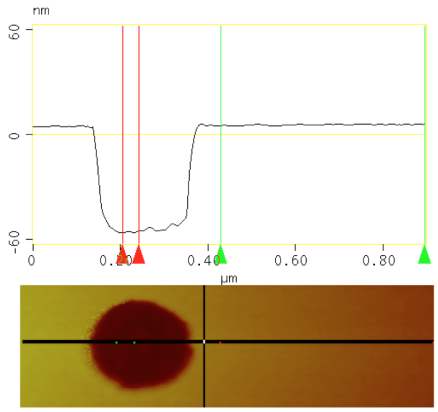

(b) A ∼250 nm wide hole, with a measured depth of 61 ± 4 nm.

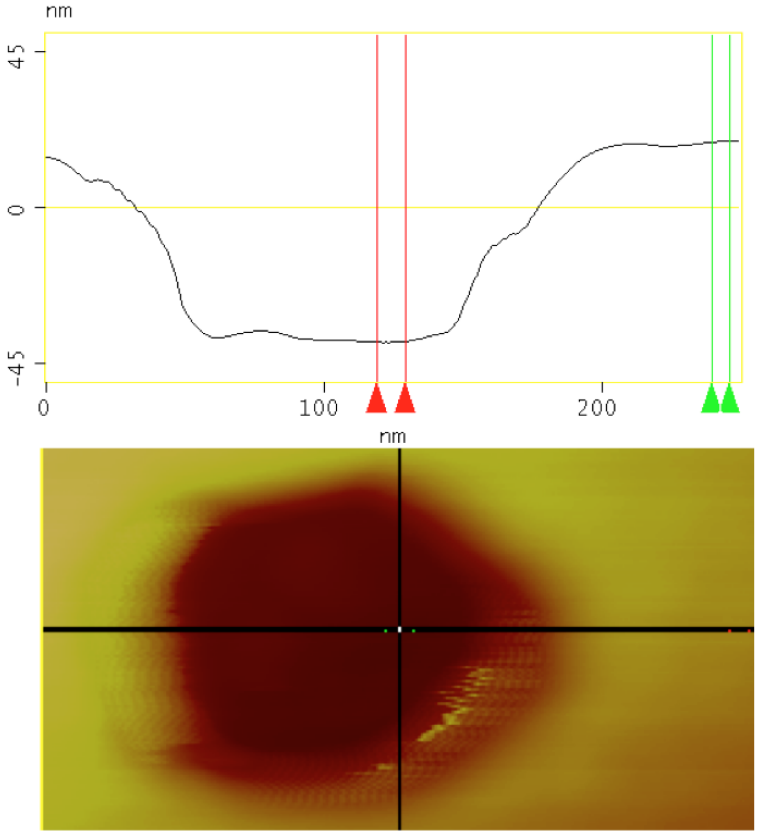

(c) A ∼200 nm wide hole, with a measured depth of 58 ± 4 nm.

Figure 24: AFM images of sample A57, which was patterned using EBL and then etched using recipe 37 for 12.5 seconds.

The depth of the 2 um wide trench on sample A57 agrees quite well with

the depths measured on PMMA drop samples (see figure 23). The hole depth and anisotropy on sample A57 begin to decrease somewhat with diameter, but they stayed in the acceptable range down to a diameter of ∼100 nm.

I used the depth measurements from sample A57 to determine an appropriate amount of Ni to deposit (using our electron beam evaporator) onto sample A58, which was patterned and then etched with sample A57 and should thus have very similar hole profiles and depths. The results of this deposition can be seen in figure 25.

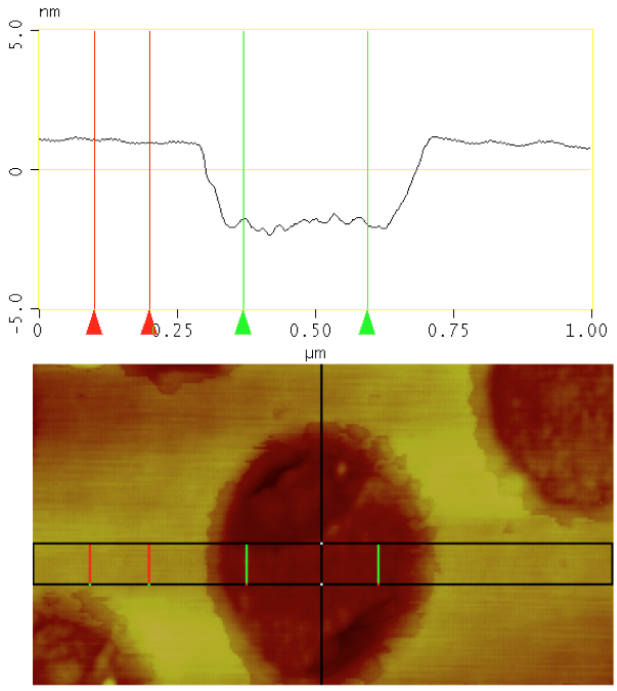

(a) A ∼420 nm diameter hole after backfilling with Ni.

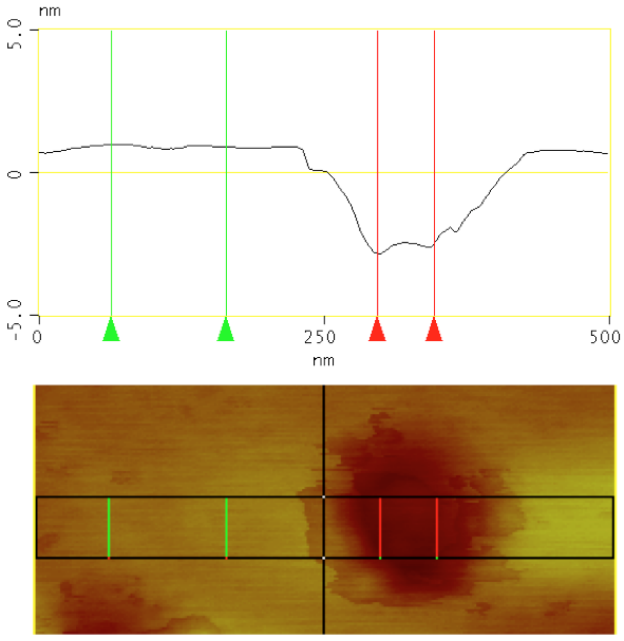

(b) A ∼200 nm diameter hole after backfilling with Ni.

Figure 25: Sample A58, which was etched with sample A57 (see figure 24) using recipe 37 for 12.5s, and then backfilled with 55 nm of Ni. Note that the vertical scale is significantly smaller than in figure 24.

The ∼420 nm diameter hole shown on the left in figure 25 was etched to an estimated depth of ∼59 nm (as measured on sample A57) and then backfilled with 55nm of Ni. The average depth of the resulting hole on sample A58 was measured to be 3 ± 1 nm, which is consistent with the expected depth (59nm - 55 nm = 4nm). Similarly, the ∼200 nm diameter hole shown on the right in figure 25 was etched to an estimated depth of ∼58 nm (again measured on sample A57) and backfilled with 55nm of Ni. The average depth of the resulting hole was measured to be 3.5 ± 1 nm, which is consistent with the expected depth (58nm - 55 nm = 3nm). This indicates that recipe 37 etched as expected, and the backfill (via electron beam evaporation) also deposited the metal fairly uniformly within the hole, as desired. A comparison of a ∼200 nm diameter hole before and after backfilling can be seen in figure 26.

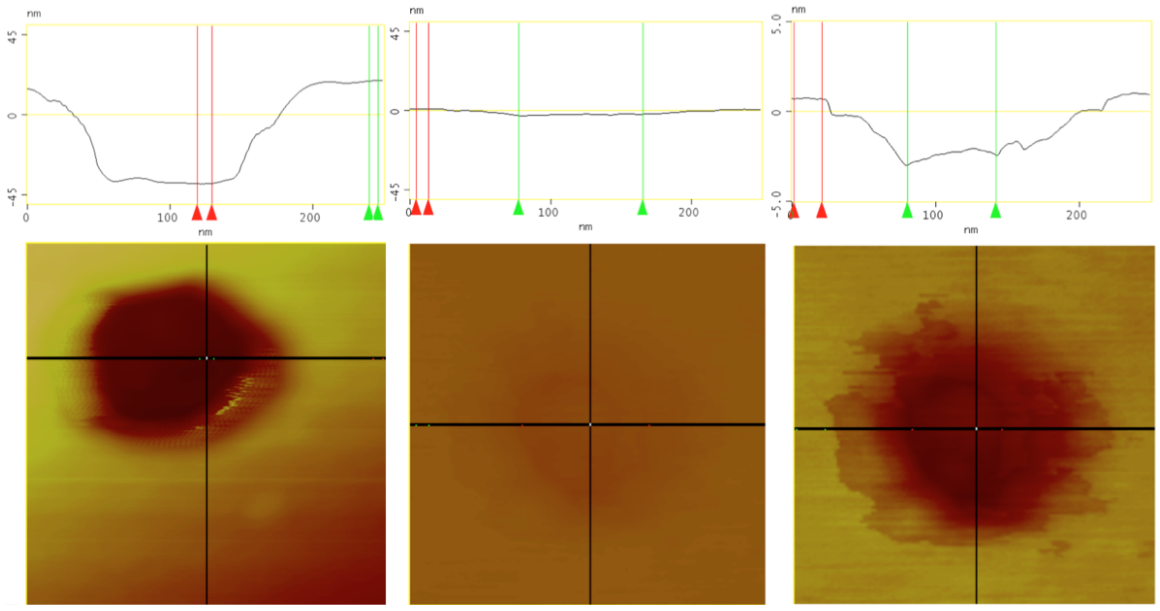

Figure 26: A comparison of ∼200 nm diameter holes before and after backfilling. Left: Before backfilling. Center: After backfilling with 55 nm of Ni (same axis scale as left image). Right: After backfilling with 55 nm of Ni (smaller axis scale than left and center images for increased visibility of small features).

I repeated this entire experiment (etching, measuring, backfilling, measuring), and the hole depths were very similar (within a nm or two of the expected depth, down to a hole diameter of ∼100nm), indicating good repeatability. Similarly, the backfill of Ni again resulted in the expected shape and depth. The average depths of the holes and the PMMA drop samples etched with recipe 37 (non dip samples only) can be seen in figure 27.

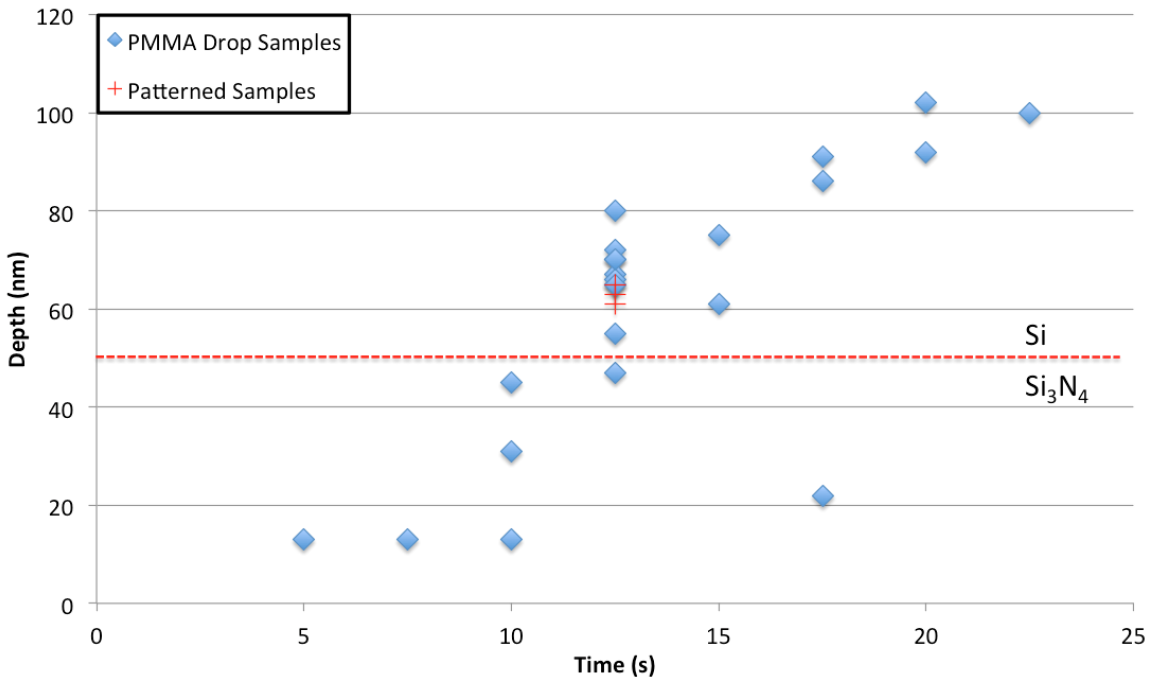

Figure 27: Depth vs. time for PMMA drop and patterned samples etched with recipe 37. The horizontal dashed red line shows the depth of the Si_3N_4 film (50 nm here).

From figure 27, it is clear that recipe 37 produces repeatable depth results on patterned samples. This indicates that I was correct that the dips would not appear

on patterned samples and provides further evidence that recipe 37 is the best candidate (or nearly so) for embedded nanomagnet/MTJ fabrication, out of all of the etching recipes possible with our RIE. In addition, this demonstrates that the sputtering, rather than the etching or another part of the fabrication process, was very likely the cause of the ring shape of the first etched MTJ sample, since I was able to achieve the desired (relatively) flat profile when backfilling with Ni via electron beam evaporation.

5.4 Embedded MTJ Fabrication Issues

MTJ stacks almost always involve layers with thicknesses of a nanometer or less. Thus, the roughness of the surfaces upon which they are deposited can prevent the MTJ from performing well or at all. Most etching roughens the surface significantly, so this poses a potential threat to the performance of any MTJ that is deposited in an etched hole. In fact, I have yet to see any recipes that consistently produced etched surfaces with RMS roughnesses less than a nm. A comparison of the RMS roughnesses of a few relevant surfaces is given in figure 28.

Feature Description	Roughness (nm)
2um Trench	2.2 ± 0.2
300nm Diameter Hole	1.7 ± 0.5
200nm Diameter Hole	1.6 ± 0.5
100nm Diameter Hole	1.3 ± 0.1
50nm SiN on Undoped Si	0.4 ± 0.1
50nm SiN on Doped Si	0.7 ± 0.1
MTJ Stack from 1st Etched MTJ Sample on 50nm SiN on Doped Si	0.9 ± 0.1
MTJ Stack on Bare Si (from previous deposition)	0.2 ± 0.1
300nm Diameter Hole Backfilled With Ni	0.3 ± 0.15
100nm Diameter Hole Backfilled With Ni	0.35 ± 0.15
Average of Holes on First Etched MTJ Sample After Backfill with MTJ Stack (only inside of hole, outer ring ignored)	2.25 ± 1

Figure 28: A comparison of the RMS roughnesses of various samples and substrates.

Looking at the top few entries in the table, roughness oddly appears to decrease with hole diameter. The cause of this is somewhat unknown, though it may be attributable to the limits of the AFM. It is conceivable that the AFM tip would have a difficult time reaching down into a small hole to accurately measure the roughness. This would place a larger uncertainty on the roughnesses of the smaller holes, despite the fact that they were measured with a Super Sharp Silicon AFM tip. In addition, the roughnesses of the smaller features are not necessarily the same as those of the larger features, so I cannot empirically determine the roughnesses of the smaller features just by measuring the larger ones (though they are likely somewhat similar).

However, assuming all the RMS roughness measurements are not larger than the true values (which is a reasonable assumption, given the nature of AFM measurements), all of the etched holes have RMS roughnesses greater than 1 nm, which would likely prevent them from acting as the substrates for growth of functional MTJs, as indicated by [17], where it is shown that TMR decreases quickly to unacceptable levels with above roughnesses of 0.4 nm.

In addition, the Si_3N_4 surface itself is too rough for fabrication of working MTJs. For comparison, a functional MTJ stack that was grown on a bare Si substrate had a final roughness of 0.2 nm. For comparison, the Si_3N_4 substrates that are grown for me on bare Si via CVD have roughnesses up to 0.7 nm. When an MTJ stack is grown on top of such a substrate, it has a roughness of 0.9 nm (which, as a sanity check, agrees with sum of the roughnesses of the Si_3N_4 substrate and the MTJ stack on bare Si).

Lastly, the roughness within the holes of the first etched MTJ sample after backfilling with a sputtered MTJ stack was $\sim 2.25 \pm 1$ nm, ignoring the outer ring area, which is probably too high to allow the material to function as an MTJ. This clearly demonstrates that the current production method will not work for making functional MTJs.

However, the roughness of the holes that were backfilled with Ni via electron beam evaporation was ~ 0.3 nm, which is relatively low, giving rise to a potential solution to the roughness problem. Instead of depositing the MTJ stack directly in the etched hole and using Ta to backfill as necessary, a layer of a nonmagnetic conductive material, such as Al or Ti, could first be deposited via electron beam

evaporation. This would serve three purposes. First, it would change the depth of the hole as needed, such that the finished MTJ stack would be flush with the top surface of the Si_3N_4. Second, it would smooth out the surface upon which the MTJ stack would be deposited, potentially solving the problem of the roughness generated by etching. Third, it would reduce or eliminate the need for additional Ta backfill. Decreasing the thickness of the Ta layer is known to decrease the roughness [18], so this could potentially create an even smoother MTJ stack.

6 Future Work

As is, the fabrication process described in figure 5 is unlikely to produce a functional MTJ, even if recipe 37 is used. Several changes could be made to this process that would increase its chances of successfully producing a working embedded MTJ.

The first of the changes is to develop and optimize the bilayer resist EBL and etching method, using recipe 37. A thorough study of the effects of different bilayer resist recipes on the EBL patterning and etching results may be necessary. This study may require several depositions via sputtering, which could be difficult, since our group does not have a sputterer.

Once the bilayer resist process is optimized, the next change would be to try adding a layer of nonmagnetic metal (Al, Ti etc) using electron beam evaporation, before the MTJ stack is sputtered onto the sample. As mentioned in the previous section, this could help smooth out the profile, adjust the hole depth and reduce the amount of Ta needed, thus potentially further reducing the roughness. The thickness

of this layer (and thus the depth of the hole needed to keep the top of the MTJ stack flush with the top of the Si_3N_4 film) would need to be adjusted to give the smoothest surface for MTJ deposition and/or the best MTJ performance.

Once the aforementioned changes to the fabrication process have been implemented successfully, another embedded MTJ sample should be produced. If the roughness and profile of MTJ's top surface are significantly better, an attempt should be made to bias this sample and measure the current, thus proving its functionality.

In addition, it may be possible to use nano etched holes filled with other metals (Ni, etc) for other applications like as BPM, etc. The process for making these samples has already been successfully demonstrated with promising results in the form of samples A58 and A62 (which was made the same way as A58, with similar results, thus proving the repeatability of this process).

7 Conclusion

I worked to establish production processes for silicon nitride-embedded MRAM and BPM. This required the development of a suitable etching recipe to create the holes in which the nanomagnetic devices could be deposited. I experimented with etching recipes that involved many combinations of $SF_6 + O_2$ and $CF_4 + O_2$ flow rates (and their implied pressures), while varying the applied power, with the goal of finding a recipe that produced repeatable depth results while maintaining a high anistropy. Though I did not try every possible recipe, I studied the parameter space effectively enough to know which combinations of parameters were likely to produce desirable

etching results. I found that recipe 37 (Power: 250W, CF_4 nominal/actual flow rate: 25/25.4 sccm, O_2 nominal/actual flow rate: 3.1/5.2 sccm, which gave a maximum pressure around 400 mTorr) was the best candidate for this role, or nearly so. I used recipe 37 as part of the production method to successfully fabricate embedded nanomagnets, which have the potential to function as embedded BPM. With a few changes to this process, embedded MTJs (and thus MRAM) could be produced.

8 Appendix A: Summary of Processes

PMMA Drop Sample	Patterned Sample (for etching and Measurement)	Patterned Sample (for etching and Deposition)	Patterned Sample (for deposition)
Prepare substrate	Prepare substrate	Prepare substrate	Prepare substrate
O2 Clean, Descum	O2 Clean, Descum	O2 Clean, Descum	O2 Clean, Descum
Apply PMMA Drop	Spin Coat	Spin Coat	Spin Coat
	Pattern	Pattern	Pattern
	Develop	Develop	Develop
Immediately before etch: O2 Clean, Descum, O2 Clean	Immediately before etch: O2 Clean, Descum, O2 Clean	Immediately before etch: O2 Clean, Descum, O2 Clean	Descum
Etch	Etch	Etch	
Remove PMMA	Remove PMMA	Deposit Metal	Deposit Metal
		Liftoff	Liftoff
AFM	AFM, repeat process for multi-material arrays	AFM, repeat process for multi-material arrays	AFM, repeat process for multi-material arrays

Prepare Sample:

1. Set hot plate to 180ºC
2. Cut samples with diamond scratch.
3. Sonicate for 3 minutes in acetone.
4. Repeat step 3 with new acetone, then with IPA.
5. Rinse with deionized H_2O, dry with N_2.
6. Dry on hotplate at 180ºC for 1 minute.

Apply PMMA Drop

1. Put PMMA drop on part of sample (use clean tweezers to minimize drop size).
2. Let cure for at least 1 hour (check that PMMA is dry).
3. Put samples on hotplate at 180ºC for 1 minute.
4. Let samples cool for at least 1 hour.

Etch

1. Warm up/clean RIE using warm up recipe for the desired etching gas.
2. Check plasma (presence and consistency), reflected power, gas flows and pressure (though this may differ from the value when a sample is in the RIE).
3. Etch samples.
4. For each new gas, do O_2 clean, repeat previous etch steps.

Remove PMMA

1. Acetone soak for at least 30 minutes, sonicate for 3 minutes in same acetone.
2. Repeat step 1 with new acetone.
3. Sonicate for 3 minutes in IPA.
4. Rinse with deionized H_2O, dry with N_2.

Spin Coat

1. Set hot plate to 180ºC
2. Line bed of spin coater with paper towel.
3. Select Recipe 8.
4. Put sample on vacuum chuck, test vacuum by starting recipe and letting it reach maximum speed. Secure larger samples to vacuum chuck with double sided tape.
5. Discard first PMMA drop, then apply PMMA to sample until surface is almost covered.
6. Run recipe.
7. Bake on hotplate at 180ºC for 1 minute.
8. Scratch sample (start in center), add a cross scratch and corner scratches.

Develop

1. Swirl in 3:7 H_2O: IPA for 1 minute.
2. Rinse with deionized H_2O, dry with N_2.

Liftoff

1. Sonicate for 3 minutes in acetone.
2. Soak in new acetone for several hours (or overnight)
3. Sonicate for 3 minutes in new acetone.
4. Sonicate for 3 minutes in IPA.
5. Rinse with deionized H_2O, dry with N_2.

Figure 29: An overview of the etching processes for fabrication of nanomagnetic devices, combined with a compact summary of the processes, for quick reference.

9 References

[1] T. R. Albrecht et al., "Bit-patterned magnetic recording: theory, media fabrication, and recording performance" IEEE Trans. Magn., vol. 51, no. 5, 2015

[2] Y. Shi, "Investigation of island geometry variations in bit patterned media storage systems", thesis, 2011, https://www.research.manchester.ac.uk/portal/files/54508266/FULL_TEXT.PDF

[3] D. Apalkov, B. Dieny, and J. M. Slaughter, "Magnetoresistive Random Access Memory", Proceedings of the IEEE, vol. 104, no. 10, pp. 17961830, 2016.

[4] A. V. Khvalkovskiy, D. Apalkov, S. Watts, R. Chepulskii, R. S. Beach, A. Ong, X. Tang, A. Driskill-Smith, W. H. Butler, P. B. Visscher, D. Lottis, E. Chen, V. Nikitin, and M. Krounbi, "Erratum: Basic principles of STT-MRAM cell operation in memory arrays", Journal of Physics D: Applied Physics, vol. 46, no. 13, p. 139601, 2013.

[5] J. Torrejon, M. Riou, F. A. Araujo, S. Tsunegi, G. Khalsa, D. Querlioz, P. Bortolotti, V. Cros, K. Yakushiji, A. Fukushima, H. Kubota, S. Yuasa, M. D. Stiles, and J. Grollier, "Neuromorphic computing with nanoscale spintronic oscillators", Nature, vol. 547, no. 7664, pp. 428431, 2017, https://www.nature.com/nature/journal/v547/n7664/pdf/nature23011.pdf

[6] "New Embedded Memories Ahead", Semiconductor Engineering. [Online]. Available: https://semiengineering.com/new-embedded-memories-ahead/. [Accessed: 03-Oct-2017].

[7] D. Shum, "CMOS-embedded STT-MRAM Arrays in 2x nm Nodes for GPMCU applications", https://www.globalfoundries.com/sites/default/files/articles/tp-cmos-embedded_stt-mram_arrays_in_2x_nm_nodes_for_gp-mcu_applications.pdf

[8] "Everspin Embedded MRAM", Everspin Embedded MRAM — Everspin. [Online]. Available: https://www.everspin.com/everspin-embedded-mram. [Accessed: 03-Oct-2017].

[9] S. H. Kang, "Non-Volatile Memories Workshop, UCSD, April 11-13, 2010", http://nvmw.ucsd.edu/2010/documents/Kang_Seung.pdf

[10] "Reactive Ion Etching (RIE)", Oxford Instruments. [Online]. Available: https:

//www.oxford-instruments.com/products/etching-deposition-and-growth/plasma-etch-deposition/rie. [Accessed: 03-Oct-2017].

[11] C. Wang and T. Suga, "Investigation of fluorine containing plasma activation for room-temperature bonding of Si-based materials", Microelectronics Reliability, vol. 52, no. 2, pp. 347351, 2012.

[12] "Reactive-ion etching", Wikipedia, 28-Apr-2017. [Online]. Available: https://en.wikipedia.org/wiki/Reactive-ion_etching. [Accessed: 03-Oct-2017].

[13] Silfes, J., Schwartz, S. (2016). "The diffraction barrier in optical microscopy" Retrieved Oct 3, 2017, from Nikon Microscopy U, http://www.microscopyu.com/techniques/super-resolution/the-diffraction-barrier-in-optical-microscopy

[14] Legtenberg, Rob and Jansen, Henri and Boer, Meint de and Elwenspoek, Miko (1995) Anisotropic reactive ion etching of silicon using $SF_6/O_2/CHF_3$ gas mixtures. Journal of the Electrochemical Society, 142 (6). pp. 2020-2028. ISSN 0013-4651

[15] "BYU Cleanroom", Silicon Nitride BYU Cleanroom. [Online]. Available: http://cleanroom.byu.edu/node/199/. [Accessed: 03-Oct-2017].

[16] H. K. Lee, K. S. Chung, and J. S. Yu, "Selective Etching of Thick Si3N4, SiO2 and Si by Using CF4/O2 and C2F6 Gases with or without O2 or Ar Addition", Journal of the Korean Physical Society, vol. 54, no. 51, p. 1816, 2009.

[17] W. Shen, D. Mazumdar, X. Zou, X. Liu, B. D. Schrag, and G. Xiao, "Effect of film roughness in MgO-based magnetic tunnel junctions", Applied Physics Letters, vol. 88, no. 18, p. 182508, 2006.

[18] M. Cecot, . Karwacki, W. Skowroski, J. Kanak, J. Wrona, A. ywczak, L. Yao, S. Dijken, J. Barna, and T. Stobiecki, "Influence of intermixing at the Ta/CoFeB interface on spin Hall angle in Ta/CoFeB/MgO heterostructures", Scientific Reports, vol. 7, no. 1, 2017. https://www.nature.com/articles/s41598-017-00994-z